MODELING OF THE DYNAMIC TRANSFORMATION ABOVE THE AE3 TEMPERATURE

MODELING OF THE DYNAMIC TRANSFORMATION ABOVE THE AE3 TEMPERATURE

BY

RYOTARO SHIRAISHI, M. Eng.

A Thesis

Submitted to the School of Graduate Studies

in Partial Fulfillment of the Requirements

for the Degree

Master of Engineering

McMaster University

© Copyright by Ryotaro Shiraishi, August 2018

MSTER OF APPLIED SCIENCE (2018) McMaster University

(Department of Materials Science and Engineering) Hamilton, Ontario

TITLE:	Modeling of the Dynamic Transformation above the Ae3 Temperature
AUTHOR:	Ryotaro Shiraishi, M. Eng. (Hokkaido University)
SUPERVISOR:	Professor Hatem S. Zurob
NUMBER OF PAGES:	xv, 93

ABSTRACT

The dynamic precipitation of ferrite during austenite deformation above the Ae3 temperature, was first reported by Yada et al. in the 1980s. These observations were later confirmed for a wide range of steel compositions and processing conditions. The aim of this work is to clarify the mechanism by which ferrite formation takes place above the Ae3 temperature. To that end, a simple model for ferrite growth as a result of the movement of disconnections under applied stress is established. This motion, opposed by the back stress, increases the Gibbs energy as a result of deformation of ferrite above Ae3. Preliminary calculation suggests that the dynamic transformation is possible near the Ae3 temperature for large stress. The results are discussed in terms of experiments using a deformation dilatometer.

ACKNOWLEDGEMENT

It has been a sincere privilege to have worked under the guidance of my supervisor, Prof. Zurob. His encouragement, enthusiasm and immense knowledge bank were utilized heavily during this work. He always found time to answer questions or discuss concerns. For everything he has done for me, I will be forever grateful. I was lucky to have him as my supervisor, and cannot imagine accomplishing as much as I have without him.

It was a pleasure to have had discussions with Prof. Purdy and his help and suggestions were greatly appreciated.

A great deal of my experiment results would not have been possible without the hard work of the canmet MATERIALS members, Dr. Fateh Fazeli, Marta Aniolek, and Tyler Smith. They operated the DIL 805D.

The lab work would have been impossible without the aid given by Jim Garrett, Doug Culley, Xiaogang Li, and Ed McCaffery. The EBSD analysis could not be completed without the kind help provided by Chris Butcher.

I have to thank for friendship to Kohei Furumai, Mukesh Sharma, Michelia Alba, and Shenglong Liang. I surely enjoyed every talk we have had, both academic and non-academic. My thanks also go to the research group of which I am honored to be a part.

I am gratefully appreciative of Nippon Steel and Sumitomo Metal Corporation, for providing the chance to study in such a splendid university and for their financial support.

Finally, I would like to thank my wife for her understanding, patience and caring over this period. Without her unwavering support this would not have been possible.

Ryotaro Shiraishi

TABLE OF CONTENTS

ABSTRACT III

ACKNOWLEDGEMENT IV

TABLE OF CONTENTS VI

LIST OF FIGURES IX

LIST OF TABLES XV

CHAPTER 1. INTRODUCTION 1

CHAPTER 2. LITERATURE REVIEW 3

2.1 EARLY INVESTIGATION OF THE DYNAMIC TRANSFORMATION 3

2.1.1. Discovery of the dynamic transformation above the Ae3 ..... *3*

2.1.2. In-situ X-ray investigations *5*

2.2 REVERSE TRANSFORMATION FROM THE DYNAMIC TRANSFORMATION FERRITE TO AUSTENITE 7

2.3 DILATOMETRY EXPERIMENT 10

2.4 LATEST MODELS OF THE DYNAMIC TRANSFORMATION 13

2.4.1. Stored energy model *13*

2.4.2. Stress activation model *17*

2.4.3. Transformation softening model *21*

CHAPTER 3. MODELING OF THE DYNAMIC TRANSFORMATION 28

3.1 DISCONNECTION MODEL 28

3.2 DRIVING FORCE 29

3.2.1. Austenite flow stress *29*

3.2.2. Internal back stress *31*

3.3 OPPOSING FORCE 33

CHAPTER 4. EXPERIMENTAL METHODS 36

4.1 DILATOMETRY EXPERIMENT 36

4.1.1. Deformation dilatometer *36*

4.2 MATERIALS 38

4.2.1. Fe–Mo–C system *38*

4.2.2. Fe–C–Mn–Si system *38*

4.3 EXPERIMENTAL PROCEDURE 39

CHAPTER 5. RESULTS 42

5.1 MODEL CALCULATIONS 42

5.1.1. Austenite flow stress *42*

5.1.2. Internal back stress *45*

5.1.3. Chemical opposing force *46*

5.1.4. Critical condition for the dynamic transformation *48*

5.2 DILATOMETRY EXPERIMENT 53

5.2.1. Dilatometry curves *54*

5.2.2. Temperature effect on dilatation *60*

5.2.3. Conversion from length data to volume fraction of ferrite *62*

5.2.4. Microstructure observation *68*

CHAPTER 6. DISCUSSIONS 71

6.1 FE–MO–C SYSTEM 71

6.1.1. Comparison of the dilatometry results and the metallography *71*

6.1.2. Validation of the model calculation *72*

6.2 Fe–C–Mn–Si system 73

6.3 Mechanism of Widmanstätten ferrite transformation 76

6.4 Effect of the dynamic recrystallization 77

6.5 Shortcoming for observing dilatation 78

6.6 Dynamic transformation in the industrial processing 80

CHAPTER 7. CONCLUSIONS 84

CHAPTER 8. FUTURE WORK 86

BIBLIOGRAPHY 90

LIST OF FIGURES

Fig. 2.1 Temperature dependence of the flow stress of steel A in Table 2.1 (Yada et al. 1986)..... 4

Fig. 2.2 Change in ferrite fraction in isothermal holding above the para equilibrium. Ae3 after hot deformation (Senuma 1988). 4

Fig. 2.3 X-Ray diffraction pattern (a) before heating, (b) at 790°C (the austenizing temperature), and (c) on the torsional deformation at 720°C (Yada et al. 2000). 6

Fig. 2.4 Optical metallography of the quenched specimens. Austenized at 790°C and (a) cooled to and held at 640°C; (b) cooled to and deformed at 640°C at a strain rate of 0.01 s^{-1}; (c) cooled to and deformed at 720°C at a strain rate of 0.01 s^{-1} and (d) cooled to and deformed at 720°C at a strain rate of 0.09 s^{-1} (Yada et al. 2000) 7

Fig. 2.5 Effect of holding time on the volume fraction (top) and grain size (bottom) of ferrite formed at various temperatures: (i) above Ae3, (ii) between Ar3 and Ae3, and (iii) below Ar3 (Senuma 1988)..... 9

Fig. 2.6 Changes in the DT ferrite morphology of a 0.13 wt% C-0.19 wt% Mn-0.49 wt% Si steel after isothermal holding for times of (a) 1 s, (b) 2 s, (c) 5 s, (d) 10 s, (e) 60 s, (f) 300 s, (g) 600 s and (h) 3600 s (Liu et al. 2007) 9

Fig. 2.7 Effect of holding time after deformation on sample dilatation for samples held at different temperatures (Senuma 1988). 12

Fig. 2.8 Dilatometry measurement of a deformed plain C steel strained to $\varepsilon = 0.3$ at 820°C with a strain rate of 10 s^{-1}. The decrease in volume indicated that the

retransformation of the dynamic transformation ferrite back into austenite occurred (Chen & Chen 2003). 12

Fig. 2.9 Dilatation curves of the specimens during isothermal holding after deformation at various temperatures above the Ae3 (Sun et al. 2008). 13

Fig. 2.10 Gibbs energy composition diagrams for the 0.79 wt% C–0.65 wt% Mn–0.24 wt% Si steel pertaining to (a) 803°C (i.e. para equilibrium Ae3 + 95°C), and (b) 863°C (i.e. para equilibrium Ae3 + 155°C). These diagrams illustrate the Gibbs energy changes taking place during the dynamic transformation (Ghosh et al. 2014). 16

Fig. 2.11 Rectangle of prior austenite ($\boldsymbol{\gamma}$) is transformed into a parallelogram of Widmanstätten ferrite ($\boldsymbol{\alpha}$) as a result of the application of a shear stress. (Jonas & Ghosh 2013) 18

Fig. 2.12 The geometry associated with the formation of a pair of "self–accommodating" plates. (Jonas & Ghosh 2013) 18

Fig. 2.13 Shear and dilatation work are added to the chemical free energy difference to indicate the dependence on temperature interval $\boldsymbol{\Delta T}$ of the total energy barrier opposing the transformation (Jonas & Ghosh 2013). 20

Fig. 2.14 Comparison between the driving force (close symbol) and the opposing force (open symbol) (Jonas & Ghosh 2013). 20

Fig. 2.15 Schematic diagram of (a) the stored energy model and (b) the mechanical activation model (Jonas & Ghosh 2013). 21

Fig. 2.16 The dependence of austenite flow stress on inverse absolute temperature (Aranas, Jr et al. 2015). 22

Fig. 2.17 The chemical free energy difference between polygonal ferrite and

austenite (solid line), and between Widmanstätten ferrite and austenite (broken line) (Aranas, Jr et al. 2015). 24
Fig. 2.18 Comparison of the driving force (solid line) and total obstacle energy (dot line) (Aranas, Jr et al. 2015). 26
Fig. 2.19 Schematic diagram of the transformation softening model (Aranas, Jr & Jonas 2015). 27
Fig. 3.1 HRTEM image of the disconnection structure at the interface between austenite and ferrite (Jiao et al. 2003). 28
Fig. 3.2 Gibbs energy difference between austenite and ferrite under (a) no diffusion of carbon, and (b) equilibrium of carbon. 34
Fig. 3.3 Gibbs energy difference between austenite and ferrite for each sample. 35
Fig. 4.1 DIL 805D deformation dilatometer. 37
Fig. 4.2 Schematic diagram of the deformation dilatometer. 37
Fig. 4.3 Schematic process diagram for (a) Fe–Mo–C system ,and (b) Fe–Mn–Si system. 41
Fig. 5.1 Stress–strain curves in of (a) Fe–Mo–C system at strain rate of 1 s^{-1} and strain range from 0 to 0.6, (b) Fe–Mo–C system at strain rate of1 s^{-1} and strain range from 0 to 0.1, (c) Steel A at strain rete of 1 s^{-1}, (d) Steel A at temperature of 880°C, (e) Steel B at strain rete of 1 s^{-1}, (f) Steel B at temperature of 880°C. 44
Fig. 5.2 Chemical Gibbs energy difference between austenite and ferrite of (a) Fe–2.4 wt% Mo–0.1 wt% C and (b) commercial steels from US Steel Canada. 47
Fig. 5.3 Comparison of the driving force and the opposing force as functions of strain. 50

Fig. 5.4 Comparison of the critical temperature for the dynamic transformation as a function of strain of the Fe–Mo–C system at strain rates ranging from 0.1 s^{-1} to 10 s^{-1} 50

Fig. 5.5 Comparison of the critical temperature for the dynamic transformation as a function of strain at strain rates ranging from 0.1 s^{-1} to 10 s^{-1} of (a) Steel A and (b) Steel B. 51

Fig. 5.6 Comparison of the critical temperature for the dynamic transformation as a function of strain rate at strain ranging from 0.1 to 0.6 of (a) Steel A and (b) Steel B. 52

Fig. 5.7 Experimental conditions at (a)Fe–Mo–C system, (b)Steel A (Fe–C–Mn–0.9 wt% Si), and (c)Steel B (Fe–C–Mn–0.5 wt% Si). 54

Fig. 5.8 Length change during isothermal holding time of Fe–Mo–C system at a strain of 0.6, strain rate of 1 s^{-1}, and various temperatures. 56

Fig. 5.9 Length change during isothermal holding time of Fe–Mo–C system at a strain of 0.1, strain rate of 1 s^{-1}, and various temperatures. 57

Fig. 5.10 Length change during isothermal holding time of Steel A at a strain of 0.6, strain rate of 1 s^{-1}, and various temperatures. 57

Fig. 5.11 Length change during isothermal holding time of steel B at a strain of 0.6, strain rate of 1 s^{-1}, and various temperatures. 58

Fig. 5.12 Length change during isothermal holding time of Steel A at a temperature of 880°C, strain rate of 1 s^{-1}, and several strains. 58

Fig. 5.13 Length change during isothermal holding time of Steel B at a temperature of 880°C, strain rate of 1 s^{-1}, and several strains. 59

Fig. 5.14 Length change during isothermal holding time of Steel A at a temperature

of 880°C, strain of 0.6, and several strain rates. 59
Fig. 5.15 Length change during isothermal holding time of Steel B at a temperature of 880°C, strain of 0.6, and several strain rates. 60
Fig. 5.16 Temperature correction on the dilatation curve for Steel A at a temperature of 880°C, strain of 0.6, and strain rate of $10s^{-1}$. 61
Fig. 5.17 Plots of length change vs. temperature used to determine the coefficient of thermal expansion from the experiments. 62
Fig. 5.18 Length difference between full ferrite and full austenite specimen as a function of temperatures. 64
Fig. 5.19 Schematic diagram of the reverse transformation. 65
Fig. 5.20 Volume fraction of ferrite at different strain levels for commercial steels. 66
Fig. 5.21 Volume fraction of ferrite at different temperatures for commercial steels. 66
Fig. 5.22 Volume fraction of ferrite at different strain rates for commercial steels. 67
Fig. 5.23 Volume fraction of ferrite at different temperatures for the Fe–Mo–C system. 67
Fig. 5.24 Optical microscopy image of Fe–Mo–C system at (a) 1060°C, ε=0.1, (b) 1000°C, ε=0.1, (c) 1100°C, ε=0.6, and (d)1040°C, ε=0.6. V_α means the volume fraction of ferrite. 69
Fig. 5.25 EBSD micrograph at 960 °C and ε=0.6 (a)band contrast image, and (b) IPF map. 70
Fig. 6.1 Comparison of model calculation and ferrite fraction of (a)Steel A (Fe–C–

Mn–0.9 wt% Si), and (b)Steel B (Fe–C–Mn–0.5 wt% Si). A mark (*) shows unreliable results. 75
Fig. 6.2 Mechanism of the ferrite formation. 76
Fig. 6.3 Influence of strain rate on the flow curves at 1100°C for a 0.25 wt%C steel (Rossard & Blain 1959). 78
Fig. 6.4 Schematic diagram of the composition of the dilatometry data. 80
Fig. 6.5 Temperature and gauge length deviations (with respect to thickness) for material exiting the roughing and finishing mills. The material is the same composition as Steel A. 82
Fig. 6.6 Temperature and strain for finishing mill 83
Fig. 6.7 Temperature reversal between finishing mills 4 to 6. 83

LIST OF TABLES

Table 2.1 Chemical compositions of the steels used in the experiments of Yada (Yada et al. 1986). 4

Table 3.1 Composition of commercial steels from US Steel Canada. 35

Table 4.1 Chemical composition of commercial steel from US Steel Canada 39

Table 4.2 Para and Ortho equilibrium temperature of the specimen 39

Table 5.1 Value of the parameter *a* and *n* in equation (3.9). 45

Table 5.2 Fitting parameters for the quadratic equation of $\Delta \mathbf{G}\boldsymbol{\alpha} - \boldsymbol{\gamma} = \boldsymbol{aT2} + \boldsymbol{bT} + \boldsymbol{c}$. Here *T* is the absolute temperature. 48

Table 6.1 Comparison of the volume fraction of ferrite between the dilatometry experiment and optical microscopy image at Fe–Mo–C system as shown in Fig. 5.20–Fig. 5.24. These numbers for the dilatometry correspond to Fig. 5.7a. 72

Chapter 1. Introduction

Phase transformation and deformation are basic phenomena involved in the solid state processes in steel. These phenomena were originally considered to be independent processes. Phase transformation is defined in terms of the temperature, time, and heating and cooling rates while deformation is associated with the strain, strain rate and temperature. In the 1960's, Thermo Mechanical Controlled Processing (TMCP) had been developed cause to combine these two phenomenon. TMCP has been used to produce steels with a wide range of mechanical properties leading to a lot of applications in various fields of industry.

It has been well understood that recrystallization and recovery can take place during and after deformation, however, the same was not known about phase transformation. This changed when, ferrite transformation from austenite during deformation was observed in 1981 (Priestner 1981). They called this "Strain Induced Transformation to Ferrite" (SITF). Other researchers make mention to this phenomenon as "Deformation Induced Ferrite Transformation" (DIFT), and "Dynamic Strain Induced Transformation" (DSIT) (Hickson 1999; Beladi et al. 2004; Dong & Sun 2005).

The final objective of the present work was to create a model for the dynamic transformation to predict the conditions neccessary for the ferrite precipitation. In

addition, the model was verified by experiment which was carried out in uniaxial hot compression testing at various temperatures, strains, and strain rates. In order to achieve this modeling goal, the mechanism of the dynamic transformation after deformation must be characterized. With this in mind, this thesis has focused on the disconnection of the atoms between two phases and considers the internal back stress from the applied stress. The following aspects of the dynamic transformation were studied in detail: the driving force; the opposing force; the reverse transformation from ferrite to austenite.

Chapter 2. Literature Review

2.1 Early investigation of the dynamic transformation

2.1.1. Discovery of the dynamic transformation above the Ae3

The dynamic transformation was widely focused by Yada's work in the 1980s (Yada et al. 1986). They carried out hot compression testing at various temperatures, strains and compositions using a high speed sequential hot deformation simulator. The chemical composition of their steels is shown in **Table 2.1**. As shown in **Fig. 2.1**, for temperatures above the Ae3 temperature the deformation stress normally increases linearly as temperature decreases. In this plot the ferrite transformation temperature was selected at the arrow mark because the deformation stress gradually decreased below this mark. The reason for this behavior is that ferrite is softer than austenite. A key point of this investigation was that the ferrite transformation temperature shifted higher as strain was increased. They found that ferrite transformation might be happening while undergoing deformation in the austenite region.

Table 2.1 Chemical compositions of the steels used in the experiments of Yada (Yada et al. 1986).

Steel	C	Si	Mn	P	S	Al	N
A	0.003	0.02	0.25	0.002	0.004	0.047	0.0011
B	0.11	0.02	1	0.003	0.002	0.019	0.0019
C	0.14	0.33	1.06	0.014	0.002	0.032	0.006

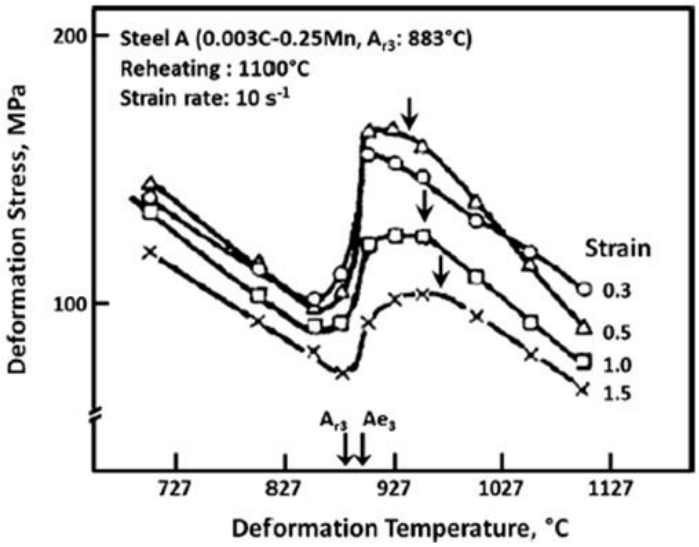

Fig. 2.1 Temperature dependence of the flow stress of steel A in **Table 2.1** (Yada et al. 1986).

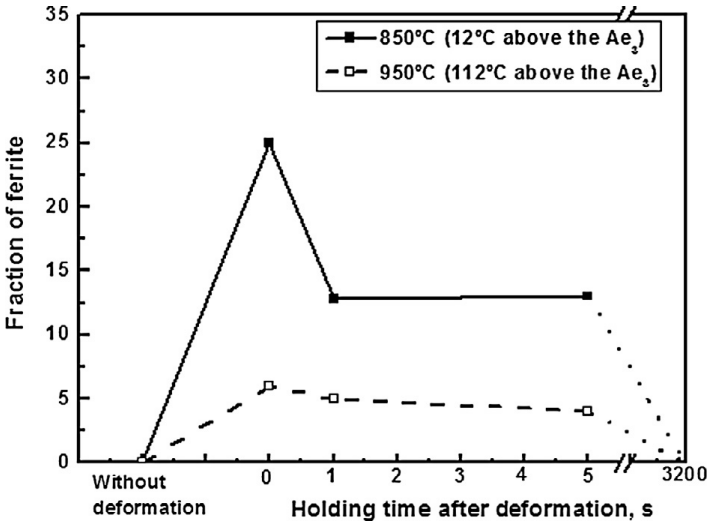

Fig. 2.2 Change in ferrite fraction in isothermal holding above the para equilibrium. Ae3 after hot deformation (Senuma 1988).

In 1988, Senuma et al. carried out isothermal holding experiments after deformation at temperatures that were above the para equilibrium temperature, i.e. 850 and 950°C (Senuma 1988). In these experiments they measured length change using a dilatometer at different values of isothermal holding time. As shown in **Fig. 2.2**, the volume fraction of ferrite was maximized immediately after deformation at both temperatures. After that, they observed a reduction of ferrite volume fraction due to the occurrence of the reverse transformation from ferrite to austenite.

2.1.2. In-situ X-ray investigations

In 2000, Yada et al. carried out in-situ experiments in order to observe the dynamic transformation directly using X-ray (Yada et al. 2000). They deformed Fe–6 wt% Ni alloy in torsion above the Ae3. The Ae3 temperature of their sample was under 700°C because of the nickel content. The advantage of the addition of nickel was that it enhanced the hardenability of the alloy. Some samples were quenched immediately after deformation to transform the austenite to martensite while preventing the reverse transformation from ferrite to austenite. Then, they were able to verify the in-situ results by comparing the result of the real time experiments and metallography.

Their experiments were carried out at temperatures over Ae3 + 40°C. As shown in **Fig. 2.3a**, the diffraction pattern corresponding to ferrite (BCC) was observed before heating. When the sample was heated up to the austenite temperature, the diffraction pattern changed from BCC to FCC, as shown in **Fig. 2.3b**. As the sample was deformed, the BCC diffraction pattern appeared again, as shown in **Fig. 2.3c**. In this study, the range of strain rates were from 0.01 to 0.09 s^{-1}. When the higher strain rates were applied to the samples, the dynamic transformation was observed at higher temperatures.

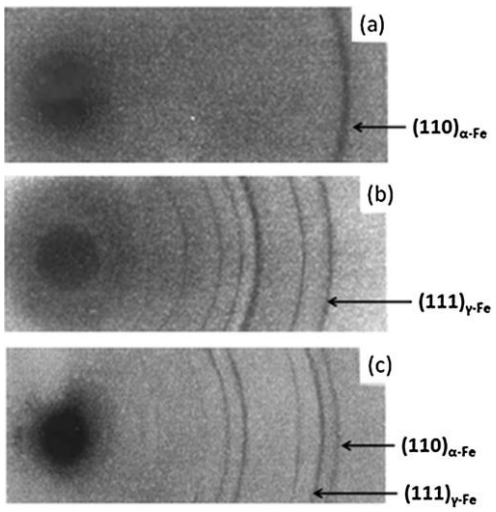

Fig. 2.3 X-Ray diffraction pattern (a) before heating, (b) at 790°C (the austenizing temperature), and (c) on the torsional deformation at 720°C (Yada et al. 2000).

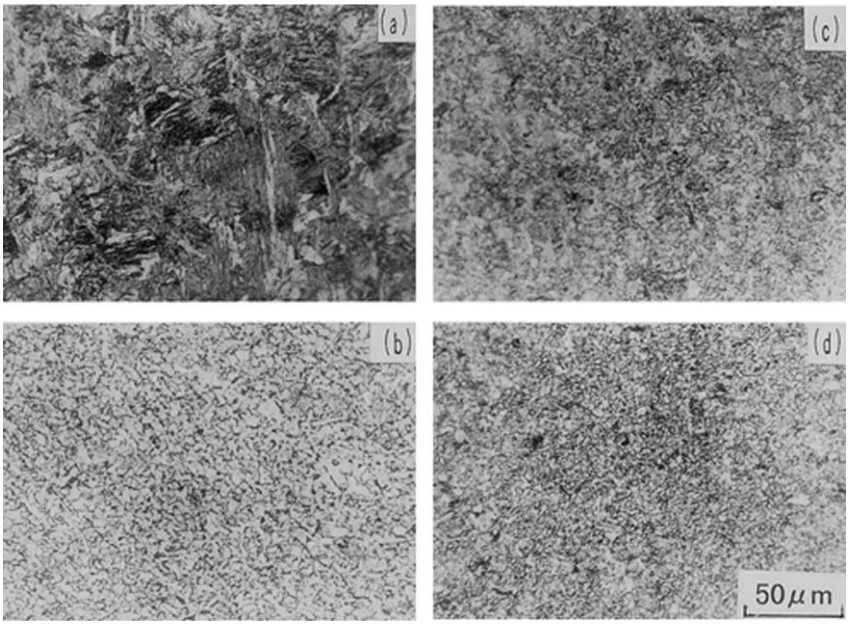

Fig. 2.4 Optical metallography of the quenched specimens. Austenized at 790°C and (a) cooled to and held at 640°C; (b) cooled to and deformed at 640°C at a strain rate of 0.01 s^{-1}; (c) cooled to and deformed at 720°C at a strain rate of 0.01 s^{-1} and (d) cooled to and deformed at 720°C at a strain rate of 0.09 s^{-1} (Yada et al. 2000)

In **Fig. 2.4**, some metallography from these experiments is exhibited. For the sample that was only austenized, cooled and held they observed martensite with some bainite structure, as seen in **Fig. 2.4a**. In this case, ferrite precipitation from the dynamic transformation has not occurred. However, for the samples that were deformed after being cooled, a large amount of precipitation was found, and was confirmed to be ferrite as observed in **Fig. 2.4b-d**.

2.2 Reverse transformation from the dynamic transformation ferrite to austenite

In 1988, Senuma et al. found that using hot strip mill simulator the dynamic transformation ferrite could be transformed back to austenite after deformation (Senuma

1988). In this study, specimens were deformed at a strain of 0.5 and strain rate of $50s^{-1}$, then quenched after several different holding times such as 0.2 s, 1 s, and 5 s. **Fig. 2.5** shows the effect of holding time on the ferrite volume fraction and grain size. The volume fraction of ferrite decreased and the grain size increased as the holding time was increased. Above the Ae3 temperature (○and●), the volume fraction of ferrite peaked immediately after deformation, and decreased after 5 seconds because of the reverse transformation from ferrite to austenite. The amount of ferrite precipitation for samples deformed above the Ae3 temperature was less than the ferrite precipitation for samples deformed at temperatures between the Ar3 and Ae3 temperatures (□) and below the Ar3 temperature (■).

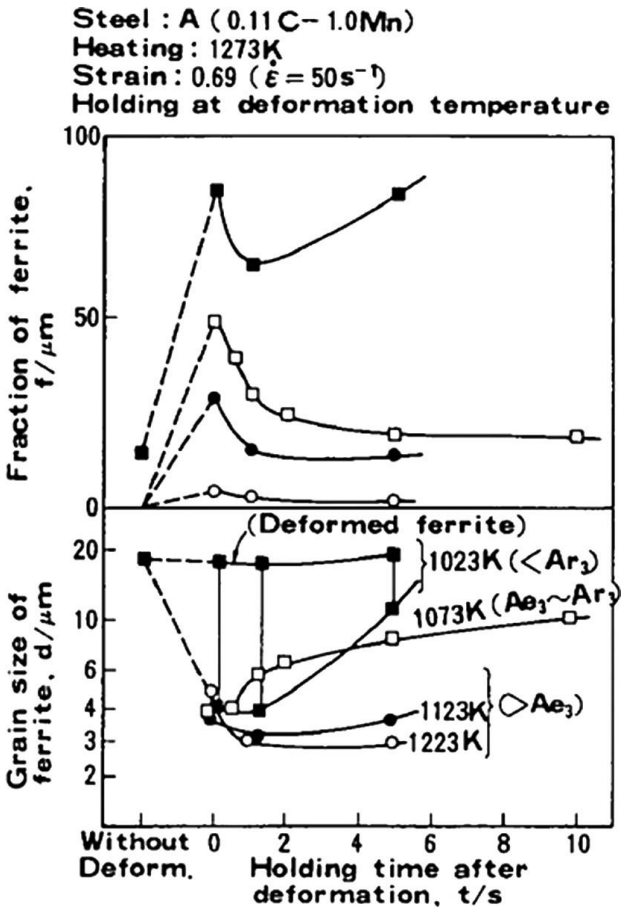

Fig. 2.5 Effect of holding time on the volume fraction (top) and grain size (bottom) of ferrite formed at various temperatures: (i) above Ae3, (ii) between Ar3 and Ae3, and (iii) below Ar3 (Senuma 1988)

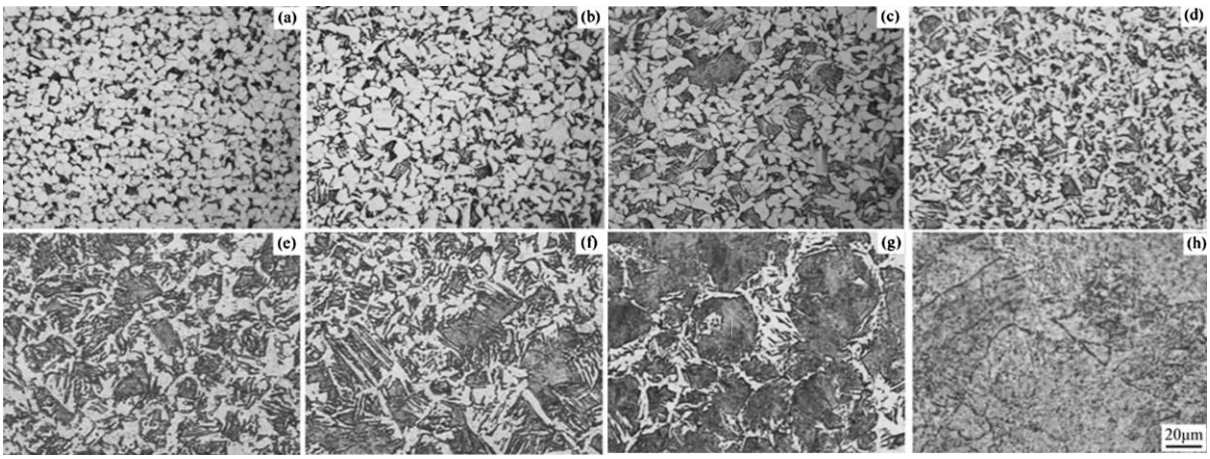

Fig. 2.6 Changes in the DT ferrite morphology of a 0.13 wt% C-0.19 wt% Mn-0.49 wt% Si steel after isothermal holding for times of (a) 1 s, (b) 2 s, (c) 5 s, (d) 10 s, (e) 60 s, (f) 300 s, (g) 600 s and (h) 3600 s (Liu et al. 2007)

The reverse transformation from ferrite to austenite was also investigated by Liu et al (Liu et al. 2007). They studied this behavior using Fe-0.13 wt% C-0.19 wt% Mn-0.49 wt% Si steel, for which the Ae3 temperature was 848°C. **Fig. 2.6** shows the microstructures of samples which were held in an isothermal condition at several different times after undergoing hot compression. In this study, the strain and strain rate were applied at 0.8 and 20 s^{-1}, respectively. As holding time increased, the ferrite grain size increased over the first five seconds as shown in **Fig. 2.6a-c**. After further holding time, the ferrite fraction decreased and changed to a martensitic structure (**Fig. 2.6d-g**). Finally, the microstructure eventually completely changed to martensite that was obtained from the austenite.

2.3 Dilatometry experiment

In order to observe the reverse transformation in real time, dilatometry experiments were performed during the isothermal holding period (Senuma 1988). As shown in **Fig. 2.7**, the reduction of dilatation corresponds to the reverse transformation from ferrite to austenite. The results of their experiments suggested that the contraction started after 3 seconds and ended after 15 seconds.

Despite the significant discovery about the dynamic transformation by Yada,

there were few follow up studies on this topic by other researchers until the 2000s. In 2003, a laser dilatometry experiment was carried out by Chen et al. to investigate the dynamic transformation (Chen & Chen 2003). As shown in **Fig. 2.8,** the contraction in dilatation is displayed until 60 seconds and gradually increases after that. They found that the forward and reverse transformation could occur simultaneously below the Ae3 temperature.

Sun et al. conducted similar dilatometric experiments in 2008 (Sun et al. 2008). Their cylindrical sample composition was Fe–0.17 wt% C–0.21 wt% Si–0.60 wt% Mn, for which the Ae3 temperature was 835°C, as calculated by Thermocalc software. They observed retransformation from ferrite to austenite under isothermal conditions after 200 seconds at both 840°C and 860°C which was at 5°C and 25°C above the Ae3 temperature of this alloy, respectively, as shown in **Fig. 2.9**. On the other hand, for the experiment carried out 950°C, which is 115°C above the Ae3, there was no signal of contraction in volume.

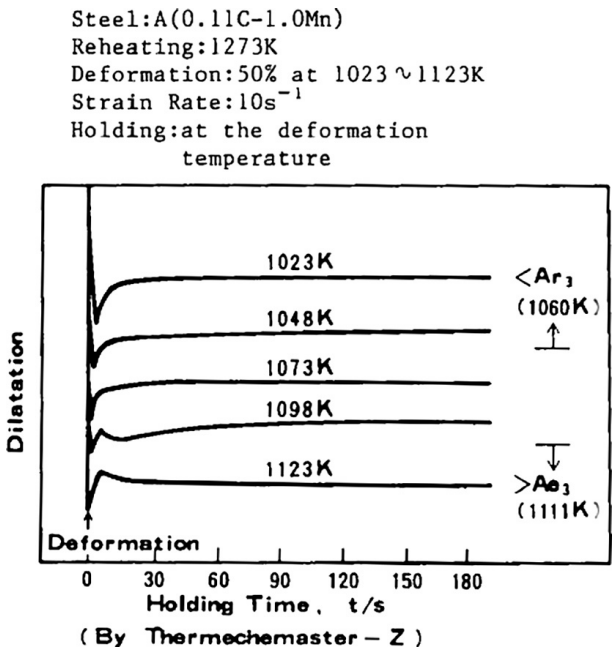

Fig. 2.7 Effect of holding time after deformation on sample dilatation for samples held at different temperatures (Senuma 1988).

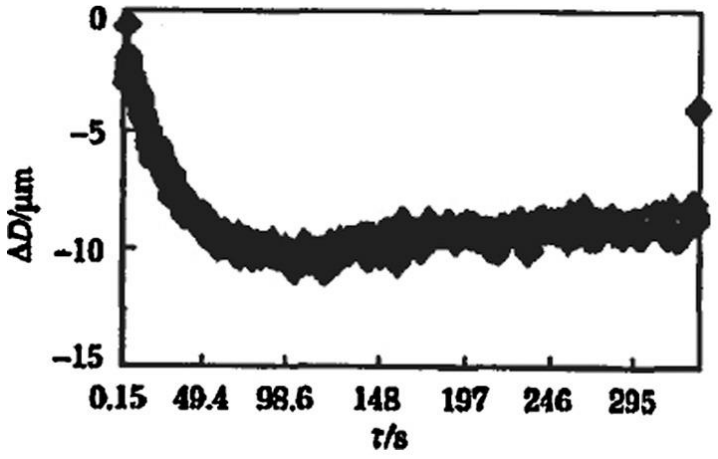

Fig. 2.8 Dilatometry measurement of a deformed plain C steel strained to $\varepsilon = 0.3$ at 820°C with a strain rate of 10 s^{-1}. The decrease in volume indicated that the retransformation of the dynamic transformation ferrite back into austenite occurred (Chen & Chen 2003).

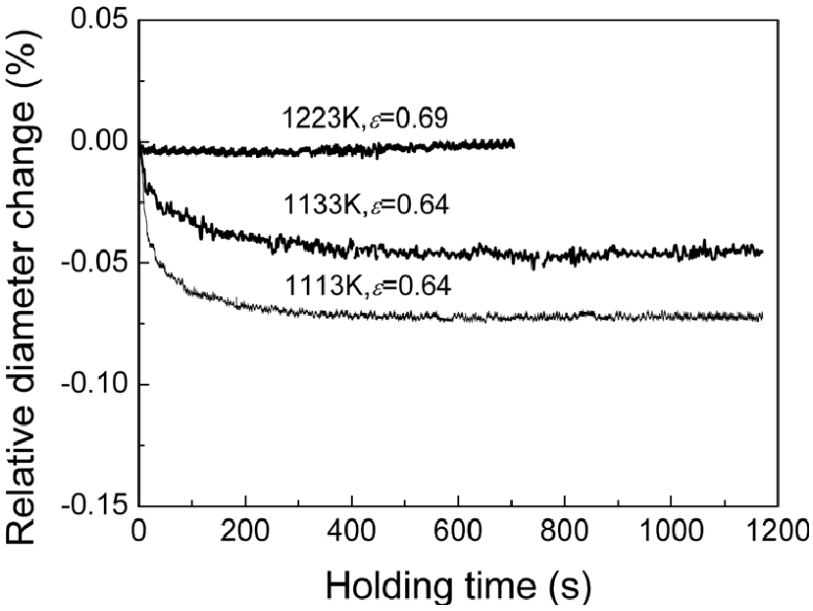

Fig. 2.9 Dilatation curves of the specimens during isothermal holding after deformation at various temperatures above the Ae3 (Sun et al. 2008).

2.4 Latest models of the dynamic transformation

Several thermodynamic models have been developed for the dynamic transformation. In the literature, there are three kinds of models: the stored energy model, the stress activation model, and the transformation softening model. These models will be reviewed briefly and including a discussion about their limitations.

2.4.1. Stored energy model

Hanlon et al. first proposed the stored energy model (Hanlon et al. 2001). The basic idea of this model is that the deformation generates stored energy and the Gibbs free energy of austenite will consequently be increased by this stored energy. When the

Gibbs free energy of austenite overcomes that of ferrite, the dynamic transformation could happen from a thermodynamic viewpoint.

The Gibbs free energy difference between austenite and ferrite is described as:

$$\Delta \boldsymbol{G} = \Delta \boldsymbol{G}^{\boldsymbol{\gamma \rightarrow \alpha}}_{\boldsymbol{Chemical}}, \tag{2.1}$$

where a negative $\boldsymbol{\Delta G}$ value means that the Gibbs energy of austenite is higher than that of ferrite. This means that ferrite is the more stable phase, which is true below the Ae3 temperature. On the other hand, above the Ae3, the Gibbs energy of ferrite is bigger than that of austenite, and therefore the austenite transformation could occur. However, when the strain is applied to the austenite above the Ae3, the stored energy increases Gibbs energy of austenite. In this case, equation (2.1) is modified as:

$$\Delta \boldsymbol{G} = \Delta \boldsymbol{G}^{\boldsymbol{\gamma \rightarrow \alpha}}_{\boldsymbol{Chemical}} - \boldsymbol{\Delta G}_{\boldsymbol{D(in\ \gamma)}}, \tag{2.2}$$

where $\Delta G_{D(in\ \gamma)}$ is the stored energy from the applied stress. When $\Delta G_{D(in\ \gamma)}$ overcomes $\Delta G^{\gamma \rightarrow \alpha}_{Chemical}$, ferrite transformation can occur above the Ae3. This stored energy consists of three components (Ghosh, Basabe, Jonas, Kim, et al. 2013; Ghosh et al. 2014):

$$\boldsymbol{\Delta G_{D(in\ \gamma)} = \Delta G_{Dislocation} + \Delta G_{Grain\ bouondary} + \Delta G_{Vacancy}}, \quad (2.3)$$

where $\Delta G_{Dislocation}$ is the dislocation line energy, $\Delta G_{Grain\ bouondary}$ is the grain boundary surface energy, and $\Delta G_{Vacancy}$ is the vacancy formation energy. These energies were defined as:

$$\boldsymbol{\Delta G_{Dislocation} = \frac{\mu_{\mathrm{T}} b_{\mathrm{T}}^2 (\rho - \rho_0)}{2}}, \quad (2.4)$$

$$\boldsymbol{\Delta G_{Grain\ bouondary} = 0.8\left[\left(S_v^{gb} + S_v^{db}\right) - S_v^0\right]}, \quad (2.5)$$

and,

$$\boldsymbol{\Delta G_{Vacancy} = Q_f C_s}, \quad (2.6)$$

where μ_{T} is the shear modulus, b_T is the Burgers vector at temperature T, ρ and ρ_0 are the dislocation densities before and after deformation, respectively, S_v^{gb} and S_v^{db} are the contributions from the grain boundaries and deformation bands, respectively, S_v^0 is the surface area in fully recrystallized austenite, Q_f and C_s are the vacancy formation energy in austenite and the excess vacancy contribution, respectively.

The effect of applying the stored energy into the Gibbs energy diagrams is illustrated in **Fig. 2.10**. **Fig. 2.10a** shows that at 95°C above the Ae3 temperature that the Gibbs energy of austenite after deformation is about 200 J/mol bigger than before deformation. **Fig. 2.10b** shows that at 155°C above the Ae3, the Gibbs free energy of

austenite after deformation is reduced by about 120 J/mol.

As described before, this model was proposed to account for the dynamic transformation. They considered the dislocations during deformation, and they could explain the transformation at 10 °C above the Ae3. After that, their model was extended to higher temperatures by distributing dislocations heterogeneously (Ghosh, Basabe, Jonas, Kim, et al. 2013; Ghosh et al. 2014). By means of this application, the stored energy model could account for the dynamic transformation as much as 100 °C above the Ae3 temperature. However, this extension required significant strain for the Gibbs energy of deformed austenite to exceed that of undeformed austenite. Such large strains are obviously insufficient to account for the dynamic transformation.

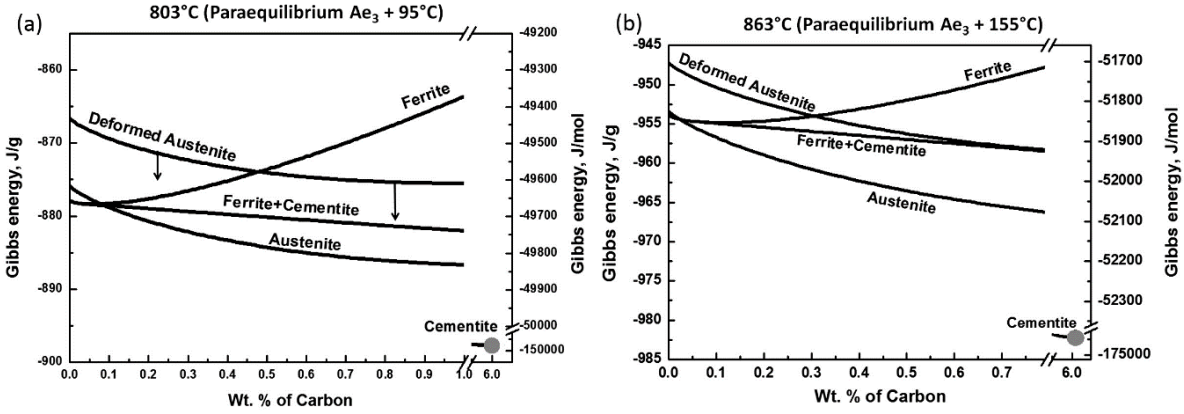

Fig. 2.10 Gibbs energy composition diagrams for the 0.79 wt% C–0.65 wt% Mn–0.24 wt% Si steel pertaining to (a) 803°C (i.e. para equilibrium Ae3 + 95°C), and (b) 863°C (i.e. para equilibrium Ae3 + 155°C). These diagrams illustrate the Gibbs energy changes taking place during the dynamic transformation (Ghosh et al. 2014).

2.4.2. Stress activation model

As described before, the stored energy model was based on dislocations, which are produced by strain instead of stress, wherein the transformation occurred when the Gibbs energy of austenite was higher than that of ferrite (Jonas & Ghosh 2013). On the other hand, the basis of the stress activation models is that the dynamic transformation happens when the applied stress overcomes the Gibbs energy barrier. This barrier is consists of three components; the chemical Gibbs energy difference between austenite and ferrite, the shear accommodation work, and the dilatation work (Ghosh, Basabe, Jonas, Kim, et al. 2013; Basabe et al. 2014; Ghosh, Basabe, Jonas, Yue, et al. 2013; Rodrigues et al. 2017).

The schematic diagram of the shear accommodation work and the dilatation work is illustrated in **Fig. 2.11**. Dilatation takes place vertical direction, which is perpendicular to the habit plane. **Fig. 2.12** shows that the austenite exists upper and lower sides on the self–accommodating plates. Since these plates extend to the right and left, it is necessary for the adjacent material to accommodate the shear from the transformation. This shear accommodation work is lower compared to the scenario in **Fig. 2.11**, as more plates form self–accommodating pairs.

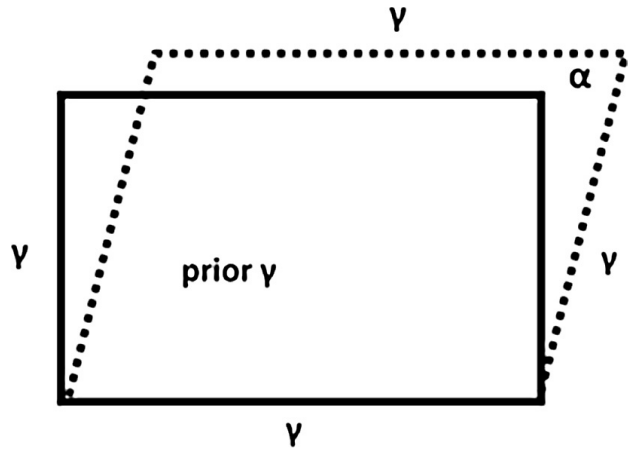

Fig. 2.11 Rectangle of prior austenite (**γ**) is transformed into a parallelogram of Widmanstätten ferrite (**α**) as a result of the application of a shear stress. (Jonas & Ghosh 2013)

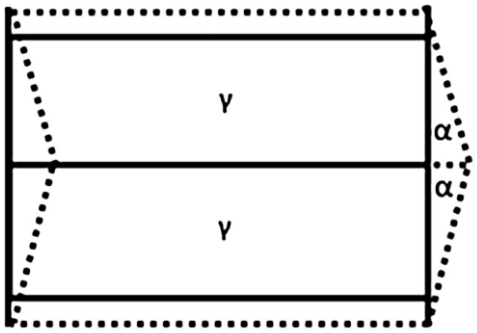

Fig. 2.12 The geometry associated with the formation of a pair of "self–accommodating" plates. (Jonas & Ghosh 2013)

The dilatation work per unit volume was described as:

$$\frac{\mathbf{W}}{\mathbf{V}} = \boldsymbol{\lambda_1 \sigma_{0.1} \varepsilon} \qquad (2.7)$$

where λ_1 is the angle between the stress axis and the habit plane normal, $\sigma_{0.1}$ is the flow stress at the nucleation of the Widmanstätten ferrite plate, and ε is the dilatation strain (Portet 2009; Bhadeshia 2001).

The shear accommodation work per unit volume was described as:

$$\frac{\mathbf{W}}{\mathbf{V}} = \boldsymbol{\tau\gamma} = \boldsymbol{m\sigma_{0.1}\gamma} \qquad (2.8)$$

where $\sigma_{0.1}$ is the flow stress at the critical strain, m is the orientation factor, and γ is a shear strain.

Finally, the total opposing force which is the sum of the chemical Gibbs energy and the shear accommodation and dilatation work is shown in **Fig. 2.13**.

On the other hand, the driving force for this model is proposed as the product of the stress, σ, and the Schmid factor, m, where the range of m is from 0.3 to 0.5. The driving force and the opposing force are illustrated in **Fig. 2.14**. The broken line shows the effect of the local stored energy of the dislocations. This figure shows that even if the stored energy of the dislocations does not contribute, the driving force for the transformation is given by the applied stress. The intersection of the lines representing the driving and opposing forces is the highest temperature at which the dynamic

transformation could happen.

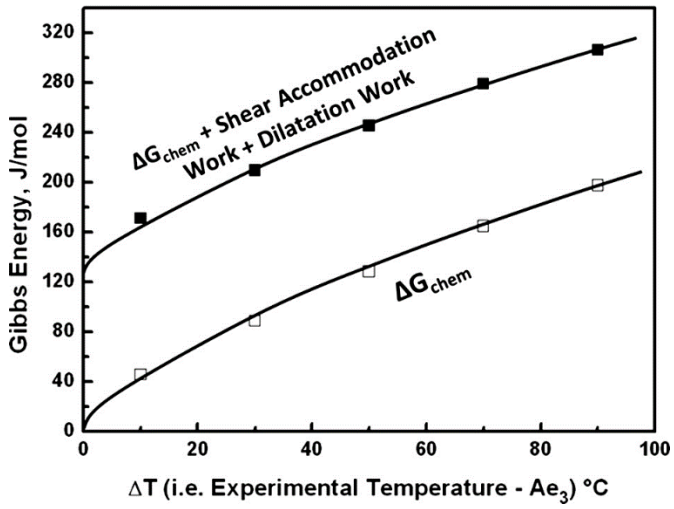

Fig. 2.13 Shear and dilatation work are added to the chemical free energy difference to indicate the dependence on temperature interval $\boldsymbol{\Delta T}$ of the total energy barrier opposing the transformation (Jonas & Ghosh 2013).

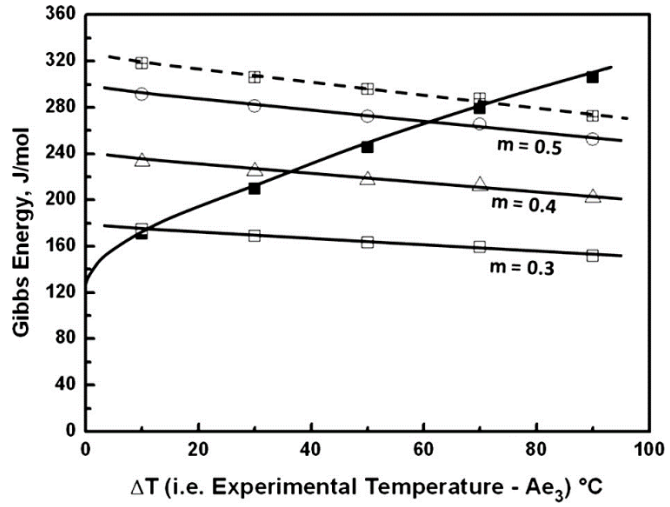

Fig. 2.14 Comparison between the driving force (close symbol) and the opposing force (open symbol) (Jonas & Ghosh 2013).

The comparison between the stored energy model and the mechanical activation

model is illustrated in **Fig. 2.15**. When the deformation increases the Gibbs energy of austenite above that of the ferrite, the austenite transforms to ferrite as shown in **Fig. 2.15a**. On the other hand, as shown in **Fig. 2.15b**, work hardening increases the deformation stress until it overcomes the sum of the chemical Gibbs energy between austenite and ferrite, the shear accommodation work, and the dilatation work.

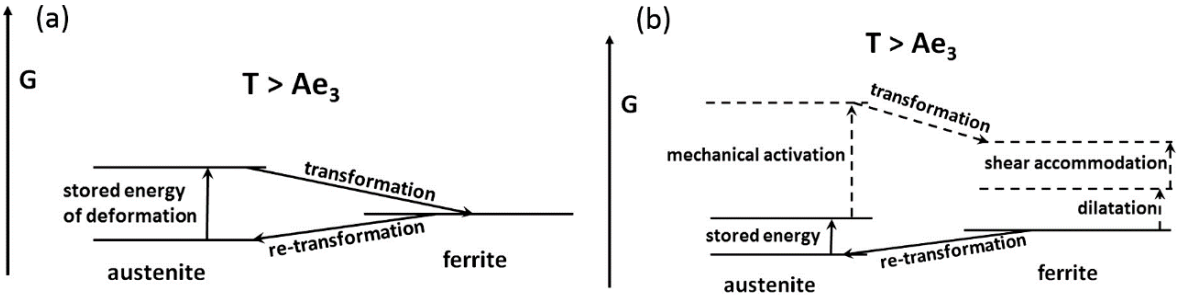

Fig. 2.15 Schematic diagram of (a) the stored energy model and (b) the mechanical activation model (Jonas & Ghosh 2013).

2.4.3. Transformation softening model

As discussed in section 2.4.2, the mechanical activation model is based on the flow stress, which works as the driving force for the transformation. On the other hand, the transformation softening model considers the softening from the Widmanstätten ferrite. The driving force is defined as the difference between the flow stress of work hardened austenite and the yield stress of the precipitated Widmanstätten ferrite (Aranas, Jr et al. 2015).

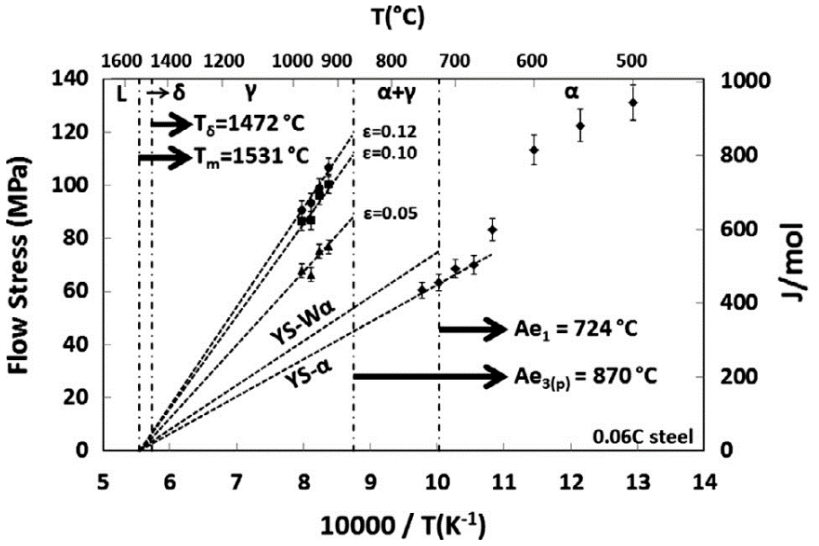

Fig. 2.16 The dependence of austenite flow stress on inverse absolute temperature (Aranas, Jr et al. 2015).

In order to estimate the yield stress of the Widmanstätten ferrite, the yield stress of the polygonal ferrite was investigated through the measurement of Vickers hardness, which was then plotted against inverse absolute temperature as shown in **Fig. 2.16**. There were two assumptions made in order to estimate the yield stress of the Widmanstätten ferrite (Aranas, Jr & Jonas 2015). First, the flow stress of the Widmanstätten ferrite fries linearly with the inverse absolute temperature similar to the polygonal ferrite. Second, the flow stress of the Widmanstätten ferrite is 18% higher than that of the polygonal ferrite.

The work hardened austenite flow stress also has a linear dependence on the

inverse absolute temperature as shown in **Fig. 2.16**. It depends on the exponential stress law for creep (Garafalo 1963):

$$\dot{\varepsilon} = Be^{C\sigma}e^{-\frac{Q}{RT}}, \tag{2.9}$$

which can be transformed as:

$$\sigma = \frac{\ln\left(\frac{\dot{\varepsilon}}{B}\right)}{C} + \frac{Q}{CR}\left(\frac{1}{T}\right), \tag{2.10}$$

where B and C are material constants, R is the universal gas constant, and Q is the activation energy.

Thus, the driving force per unit volume is described as:

$$\left(\frac{W}{V}\right)_{driving\ force} = (\sigma_\gamma - \sigma_{wf})m, \tag{2.11}$$

where σ_γ is the flow stress of work hardened austenite, σ_{wf} is the yield stress of the Widmanstätten ferrite, and m is Schmid factor.

The opposing force of this model consists of the chemical Gibbs energy between

the two phases, shear accommodation, and dilatation work (Aranas, Jr & Jonas 2015; Jonas & Ghosh 2013). The Gibbs energy difference between austenite and ferrite is illustrated in **Fig. 2.17**. This figure suggests that the transformation from austenite to Widmanstätten ferrite requires 5 to 15 J/mol of free energy more than is required for the transformation from austenite to polygonal ferrite.

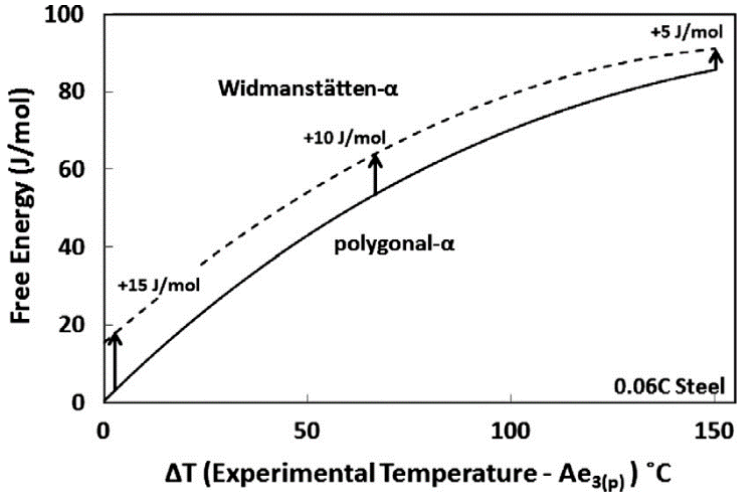

Fig. 2.17 The chemical free energy difference between polygonal ferrite and austenite (solid line), and between Widmanstätten ferrite and austenite (broken line) (Aranas, Jr et al. 2015).

The shear accommodation and dilatation work are also required for the transformation of austenite to Widmanstätten ferrite, as previously described in 2.4.2. Here, the transformation involves a shear strain of 0.36 and a dilatation 0.03, which is perpendicular to the habit plane (Watson 1973), as shown in follows:

$$\left(\frac{W}{D}\right)_{S.A.} = 0.36 m \sigma_c \tag{2.12}$$

$$\left(\frac{W}{D}\right)_{D} = 0.03 \lambda \sigma_c \tag{2.13}$$

where m is the Schmid factor, λ is the orientation factor, and σ_c is the flow stress at the critical strain for the dynamic transformation.

The comparison between the driving force, shown in **Fig. 2.17**, and the total energy obstacles for a strain of 0.12 are shown in **Fig. 2.18**. The total energy barrier is calculated as the sum of the chemical Gibbs energy, the shear accommodation work, and the dilatation work as follows:

$$\textbf{Total Energy Barrier} = \Delta G_{\gamma - W\alpha} + \left(\frac{W}{V}\right)_{S.A.} + \left(\frac{W}{V}\right)_{D} \tag{2.14}$$

The point of intersection of the driving force and the energy barrier represents the maximum temperature for which the dynamic transformation occurs. This figure suggests that the dynamic transformation can happen at temperatures up to 54°C above the Ae3 at a strain of 0.12. A schematic diagram of the transformation softening model is illustrated in **Fig. 2.19**. Above the Ae3 temperature, austenite is the stable phase because the austenite Gibbs energy is lower than that of ferrite. When the deformation

is applied to austenite and its flow stress is enough to exceed the energy barrier for the transformation, the dynamic transformation to Widmanstätten ferrite can take place. After releasing the stress, the ferrite reverse transforms to austenite by a slower diffusional process (Ghosh, Basabe, Jonas, Kim, et al. 2013; Ghosh et al. 2014).

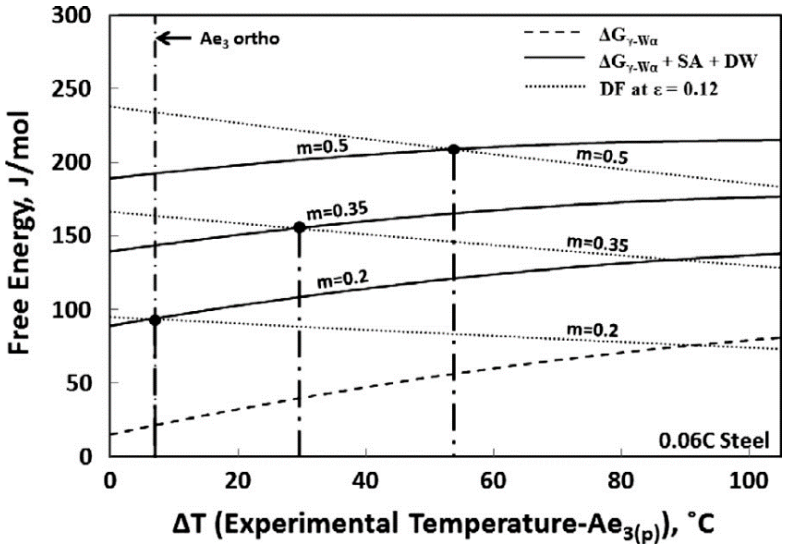

Fig. 2.18 Comparison of the driving force (solid line) and total obstacle energy (dot line) (Aranas, Jr et al. 2015).

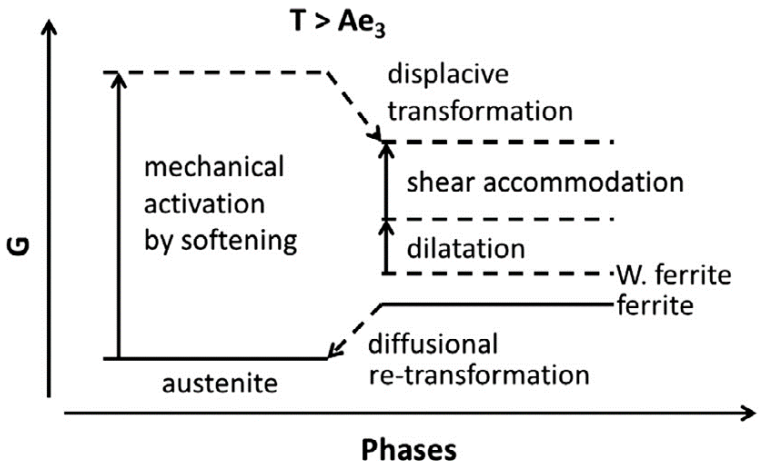

Fig. 2.19 Schematic diagram of the transformation softening model (Aranas, Jr & Jonas 2015).

Chapter 3. Modeling of the Dynamic Transformation

In this chapter, the details of the model which we propose will be introduced. This model consists of two components: the driving force and the opposing force.

3.1 Disconnection model

The basic concept of the model which we propose revolves around the idea that the interface between ferrite and austenite consists of dislocations and disconnections, which is a misfit for arrays of atoms as shown in **Fig. 3.1** (Howe et al. 2009). Howe et al. suggested that the transformation proceeds by the movement of these disconnections. When the material is deformed, an internal shear stress is applied to the interface. This shear stress can cause the disconnections to move and the transformation can occur.

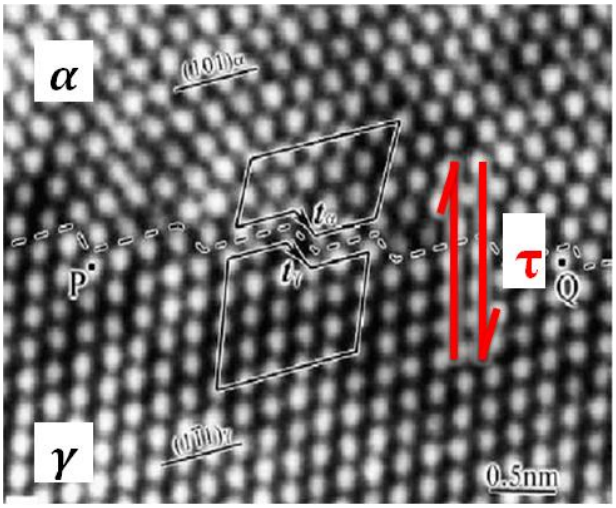

Fig. 3.1 HRTEM image of the disconnection structure at the interface between austenite and ferrite (Jiao et al. 2003).

3.2 Driving force

One of the key requirements for this model is that we need to estimate the driving force for the dynamic transformation. The driving force of this model is described as:

$$\textbf{Driving force} = (\sigma_\gamma - \hat{\sigma})m\frac{b}{L}, \tag{3.1}$$

where σ_γ is the austenite flow stress, $\hat{\sigma}$ is an internal back stress, m is the Schmid factor, b is the magnitude of the Burgers vector, and L is the mean free distance of a mobile dislocation.

3.2.1. Austenite flow stress

Medina et al. proposed an empirical model for the austenite flow stress at the hardening and dynamic recovery region, which can be written as (Medina & Hernandez 1992; Hernandez et al. 1996):

$$\sigma_e = B[1 - \exp(-C\varepsilon)]^m, \tag{3.2}$$

where *B*, *C*, *m* are calculated for this empirical equation as (Hernandez et al. 1996):

$$\boldsymbol{B = \left(9.5326 + 0.6196 ln \frac{Z}{A}\right)^2}, \tag{3.3}$$

$$\boldsymbol{C = 3.9202 \left(\frac{Z}{A}\right)^{0.0592}}, \tag{3.4}$$

$$\boldsymbol{m = 0.3449 \exp\left(0.0139 \sqrt{\frac{Z}{A}}\right)}. \tag{3.5}$$

The Zener–Hollomon Parameter (*Z*) used in these equations was first proposed by Zener and Hollomon (Zener & Hollomon 1944), wherein the stress–strain relationship depends on the strain rate and temperature at the isothermal condition, and can be defined as:

$$\mathbf{Z = \dot{\varepsilon} \exp\left(\frac{Q}{RT}\right)}, \tag{3.6}$$

where *Q* is the activation energy for hot deformation, *R* is the gas constant (8.318 J/mol/K), and *T* is the absolute deformation temperature. Medina et al. modeled the activation energy *Q* using an empirical equation based on alloy composition (Medina & Hernandez 1996), which was defined as:

$$\boldsymbol{Q = 26700 - 2535.52(wt\%\ C) + 1010(wt\%\ Mn) + 33620.76(wt\%\ Si) + 35651.28(wt\%\ Mo) + 93680.52(wt\%\ Ti)^{0.5919} + 31673.46(wt\%\ V) + 70729.85(wt\%\ Nb)^{0.5649}.} \quad (3.7)$$

The results of the calculation using (3.7) were good approximation with a correlation coefficient of 0.996 (Medina & Hernandez 1996).

Parameter *A*, from equation (3.3)–(3.5), was expressed using an exponential equation by Medina et al., as follows:

$$\boldsymbol{A = [12.197 + 65.590(wt\%\ C) - 49.052(wt\%\ Nb)]\exp(7.076 \times 10^{-5} Q)}. \quad (3.8)$$

In our model, the equation of the austenite flow stress, σ_γ, introduces fitting parameters *a* and *n* in order to better fit the experimental stress–strain curve. This equation can be written as:

$$\boldsymbol{\sigma_\gamma = aB[1 - \exp(-C\varepsilon)]^{m/n}}. \quad (3.9)$$

3.2.2. Internal back stress

The driving force of our model for the dynamic transformation requires the internal back stress to be estimated.

Estrin et al. investigated a constitutive model that related the dislocation density to the internal back stress (Estrin 1996). They started their model with the kinetic equation by Kocks (Kocks 1976):

$$\dot{\boldsymbol{\varepsilon}}^{\boldsymbol{p}} = \dot{\boldsymbol{\varepsilon}}_{\mathbf{0}} \left(\frac{\boldsymbol{\sigma}}{\hat{\boldsymbol{\sigma}}} \right)^{\boldsymbol{m}}, \tag{3.10}$$

where $\dot{\varepsilon}^p$ is the plastic part of strain rate, $\hat{\sigma}$ is the internal back stress, and $\dot{\varepsilon}_0$ and m are material parameters.

Estrin stated that the relationship between a transient strain ε_{tr} and a saturation stress σ_s can be shown as:

$$\boldsymbol{\sigma_s = \Theta_{II} \varepsilon_{tr}}, \tag{3.11}$$

where Θ_{II} is the stage II hardening rate, which can be described as:

$$\boldsymbol{\Theta_{II} = \frac{1}{2} M^2 \alpha G b k_1 \left(\frac{\dot{\varepsilon}^p}{\dot{\varepsilon}_0} \right)^{\frac{1}{m}}}. \tag{3.12}$$

Here G is the shear modulus, and α is a numerical constant. The equations from (3.10)–(3.12) can be combined to give:

$$\boldsymbol{\frac{\sigma}{\hat{\sigma}} = \frac{2}{M^2 \alpha G b k_1} \frac{\sigma_s}{\varepsilon_{tr}}}. \tag{3.13}$$

Here, σ_s and ε_{tr} originate from the Voce law (Voce 1948), which is an empirical model to describe strain hardening behavior, and is written as:

$$\boldsymbol{\sigma = \sigma_s \left[1 - \exp\left(-\frac{\varepsilon}{\varepsilon_{tr}}\right)\right]}. \quad (3.14)$$

This equation form is similar to equation (3.2) with the exception of the m_{th} power. Here, if an assumption is considered that m equals to 1 in equation (3.2), σ_s and ε_{tr} are equal to B and $1/C$, respectively.

Therefore, the internal back stress $\hat{\sigma}$ that causes the deformation in the austenite region is described as:

$$\boldsymbol{\hat{\sigma} = \sigma_\gamma \frac{M^2 \alpha G b k_1}{2BC}}. \quad (3.15)$$

3.3 Opposing force

The most important obstacle to the formation of ferrite above the Ae3 temperature is the chemical Gibbs energy difference between the FCC and BCC phases. The chemical Gibbs energy can be calculated using the *Thermocalc* software with the TCFE6 data–base. After calculating the Gibbs energy difference between FCC and BCC, a quadratic approximation was fitted to the result.

There are two ways to estimate the opposing force. One way is based on a

condition with no diffusion of carbon, and the other way is based on condition of equilibrium of carbon, as shown in **Fig. 3.2**.

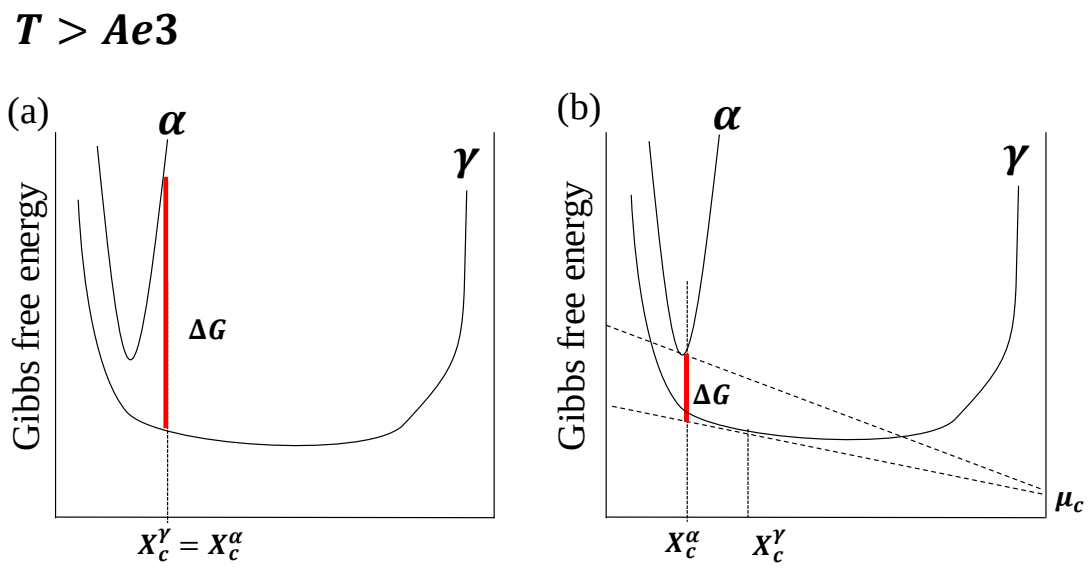

Fig. 3.2 Gibbs energy difference between austenite and ferrite under (a) no diffusion of carbon, and (b) equilibrium of carbon.

The Gibbs energy difference of three different commercial steels, whose compositions are shown in **Table 3.1**, was calculated using each of the two ways presented in **Fig. 3.2**. **Fig. 3.3** shows the Gibbs energy difference between austenite and ferrite for each of these steel samples. A positive Gibbs energy difference means a stable austenite phase and the ferrite transformation doesn't happen. Based on observations in industrial settings, more dynamic transformation can happen when steels have a higher silicon component. On the other hand, lower silicon steels show small amounts of the dynamic transformation. For this reason, the calculation method based on carbon

diffusion is more reasonable for our model.

Table 3.1 Composition of commercial steels from US Steel Canada.

Steel	C	Si	Mn	P	S	Cu	Al	Cr
A	0.09	0.89	1.97	0.012	0.003	0.025	0.040	0.036
B	0.17	1.46	2.04	0.017	0.002	0.036	0.044	0.041
C	0.05	0.51	1.63	0.010	0.003	0.023	0.042	0.029

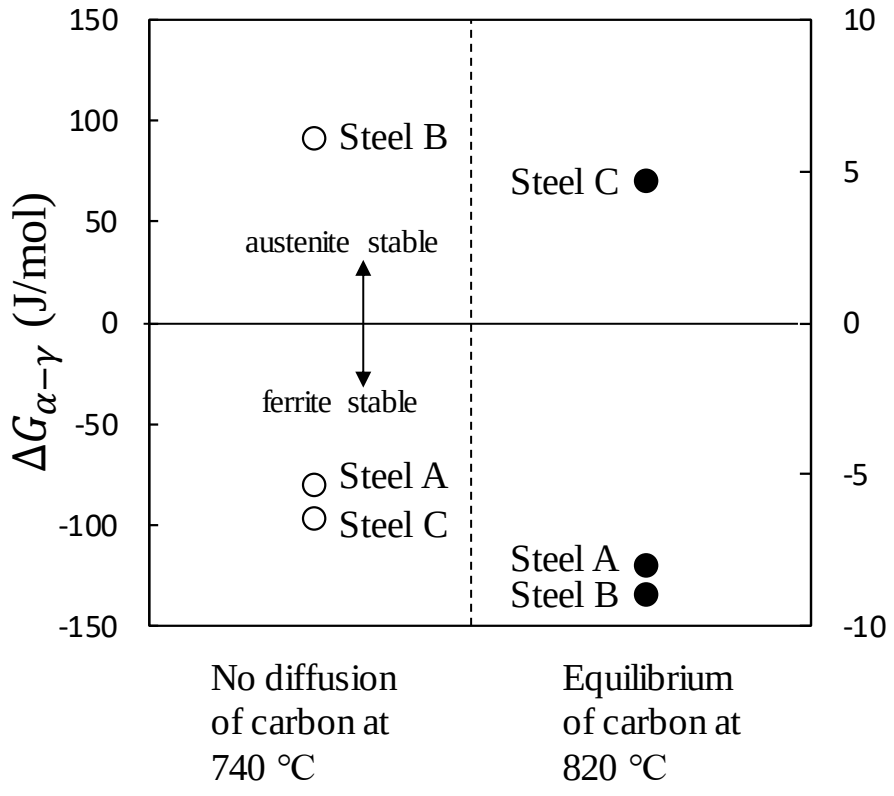

Fig. 3.3 Gibbs energy difference between austenite and ferrite for each sample.

Chapter 4. Experimental Methods

In this chapter, the details of the experimental work will be introduced. To validate the model which we proposed in Chapter 3, two different steel alloys were used.

4.1 Dilatometry experiment

The dynamic transformation was observed by dilatometry experiments. This method was first used by Senuma et al (Senuma 1988) for measuring volume change under isothermal conditions. After that, the dilatometry experiment was used to investigate the dynamic transformation in a number of research studies, as discussed in section 2.3.

4.1.1. Deformation dilatometer

This experimental work was carried out using a DIL 805D deformation dilatometer, as shown in **Fig. 4.1**, and was used for measuring length change during isothermal holding times.

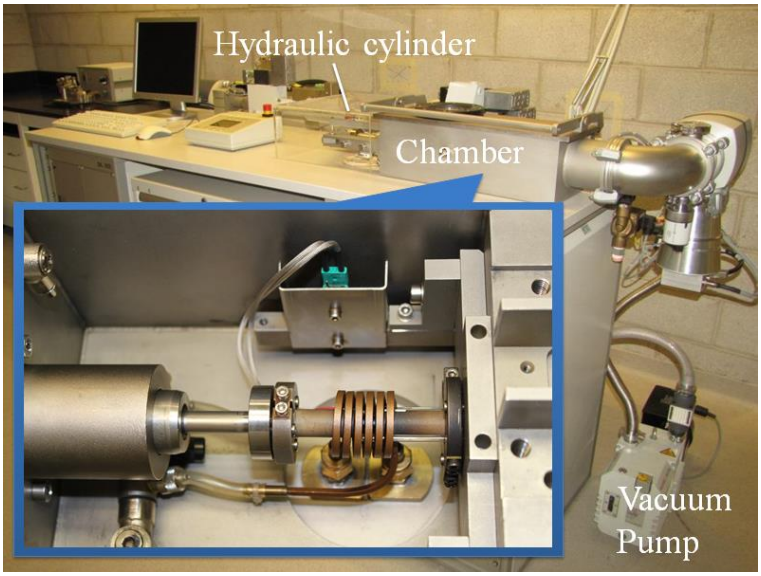

Fig. 4.1 DIL 805D deformation dilatometer.

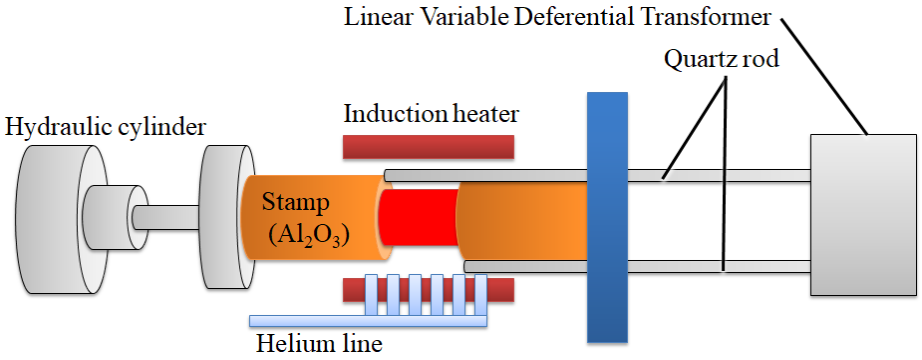

Fig. 4.2 Schematic diagram of the deformation dilatometer.

The specimen is fixed in place between two alumina stamps and heated up by an induction heater. It is then compressed by a hydraulic cylinder and quenched by helium gas. The length change is measured by quartz rods, and calculated by the linear variable deferential transformer (LVDT). A K–type thermocouple was welded on the surface of the center in length direction of the samples to measure and record the sample

temperature. During the testing, the chamber was under vacuum until the quenching step at the end of the heating cycle. All tests were carried out at CANMET Materials (Hamilton, ON).

4.2 Materials

4.2.1. Fe–Mo–C system

The chemical composition of the model alloy that was used in our experiment is Fe–2.4 wt% Mo–0.1 wt% C. Molybdenum was added to enhance the hardenability of the sample to aid in validating the results from the dilatometer with the results from metallography. The sample was cast by arc melting, then hot rolled from 13 mm to 6.5 mm using 7 passes at 900 °C in order to remove the dendrite structure. Cylindrical compression specimens, which were 5 mm in diameter and 10 mm in length, were machined after the hot rolling of the sample. The ortho equilibrium temperature and the para equilibrium temperature of this sample are 945°C and 930°C, respectively.

4.2.2. Fe–C–Mn–Si system

The other system is a commercial steel from US Steel Canada with a chemical composition as shown in **Table 4.1**. Cylindrical compression specimens of this alloy,

which were 5 mm in diameter and 10 mm in length, were also machined. The Ae3 temperatures of para equilibrium and ortho equilibrium are shown in **Table 4.2**, which was calculated by *Thermocalc* software with the TCFE6 data–base.

Table 4.1 Chemical composition of commercial steel from US Steel Canada

Steel	C	Si	Mn	P	S	Cu	Al	Cr
A	0.09	0.89	1.97	0.012	0003	0.025	0.40	0.036
B	0.05	0.51	1.63	0.010	0.003	0.023	0.42	0.029

Table 4.2 Para and Ortho equilibrium temperature of the specimen

Steel	Para E (°C)	Ortho E (°C)
A	810	840
B	826	850

4.3 Experimental procedure

The schematic experimental process diagrams are shown in **Fig. 4.3**. The samples were heated at the rate of 5°C/s up to 1200°C for homogenizing austenite and then held for 2 minutes to ensure that the transformation to austenite was completed. The samples were then cooled at 10°C/s down to test temperatures and held for 5 seconds before deformation. The samples were compressed to strains of 0.1, 0.3, or 0.6 at strain rates of $0.1s^{-1}$, $1\ s^{-1}$, or $10\ s^{-1}$. After the deformation, the applied force was removed immediately. Over a holding period of 10 seconds, during which the ample could re-

transform from ferrite to austenite, the length change of the samples was measured. The samples were then subsequently quenched with helium gas. As shown in **Fig. 4.3a**, some specimens were quenched immediately after deformation in order to observe the microstructure. These samples were cut along the compression direction, and etched using 2% nitric acid in ethanol in order to obtain the optical microscopy images.

The EBSD analysis for Widmanstätten ferrite was made on a JEOL JSM–7000F FEG–SEM with a CCD detector. An accelerating voltage of 20 kV, a tilt angle of 70°, a step size of 0.1 μm, and a grid of 1704×1278 were used for EBSD analysis.

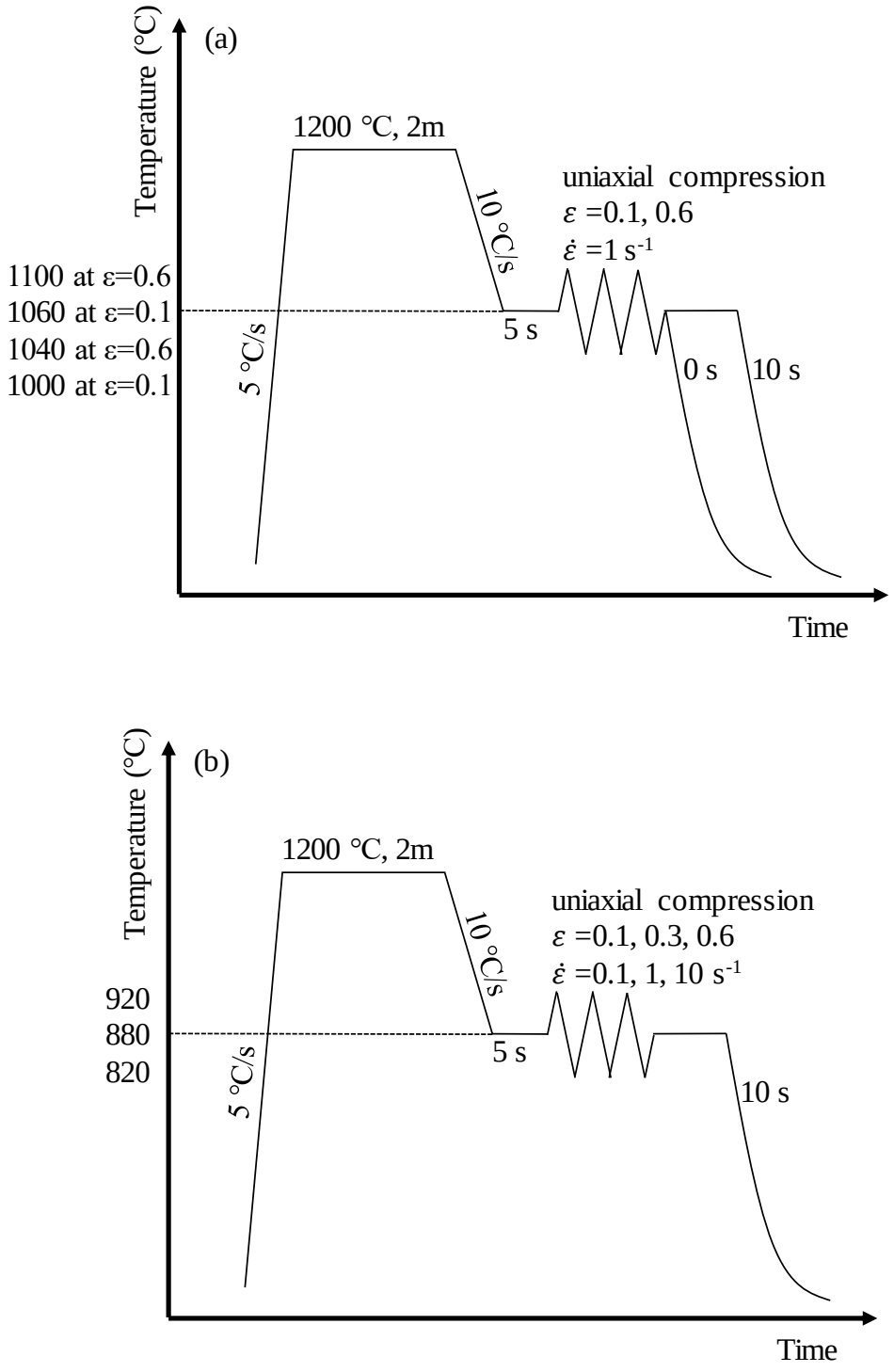

Fig. 4.3 Schematic process diagram for (a) Fe–Mo–C system ,and (b) Fe–Mn–Si system.

Chapter 5. Results

In this chapter, the results of the calculations using model presented in Chapter 3 and the experimental results of the tests using dilatometer will be summarized. The model calculations, experimental results for the Fe–Mo–C system and experimental results for the Fe–C–Mn–Si system, are presented in section 5.1, 5.2, and 5.3, respectively.

5.1 Model calculations

The modeling calculations were performed using the *Maple* software. The specimens for these calculations were the same as those shown in Chapter 4, which are Fe–2.4 wt% Mo–0.1 wt% C, Fe–1.97 wt% Mn–0.89 wt% Si–0.09 wt% C, and Fe–1.63 wt% Mn–0.51 wt% Si–0.05 wt% C.

5.1.1. Austenite flow stress

The austenite flow stress was calculated using equation (3.9) and was compared to the experimental stress–strain curves as illustrated in **Fig. 5.1**. The flow stress for a given alloy was found to be higher for lower temperatures and higher strain rates. The values of the parameters a and n are listed in **Table 5.1**. These parameters were

determined by comparing the model calculation for a given system to the corresponding experiment and selecting parameter values such that the difference between the experimental stress–strain curve and the results of calculation had a maximum error of 5%.

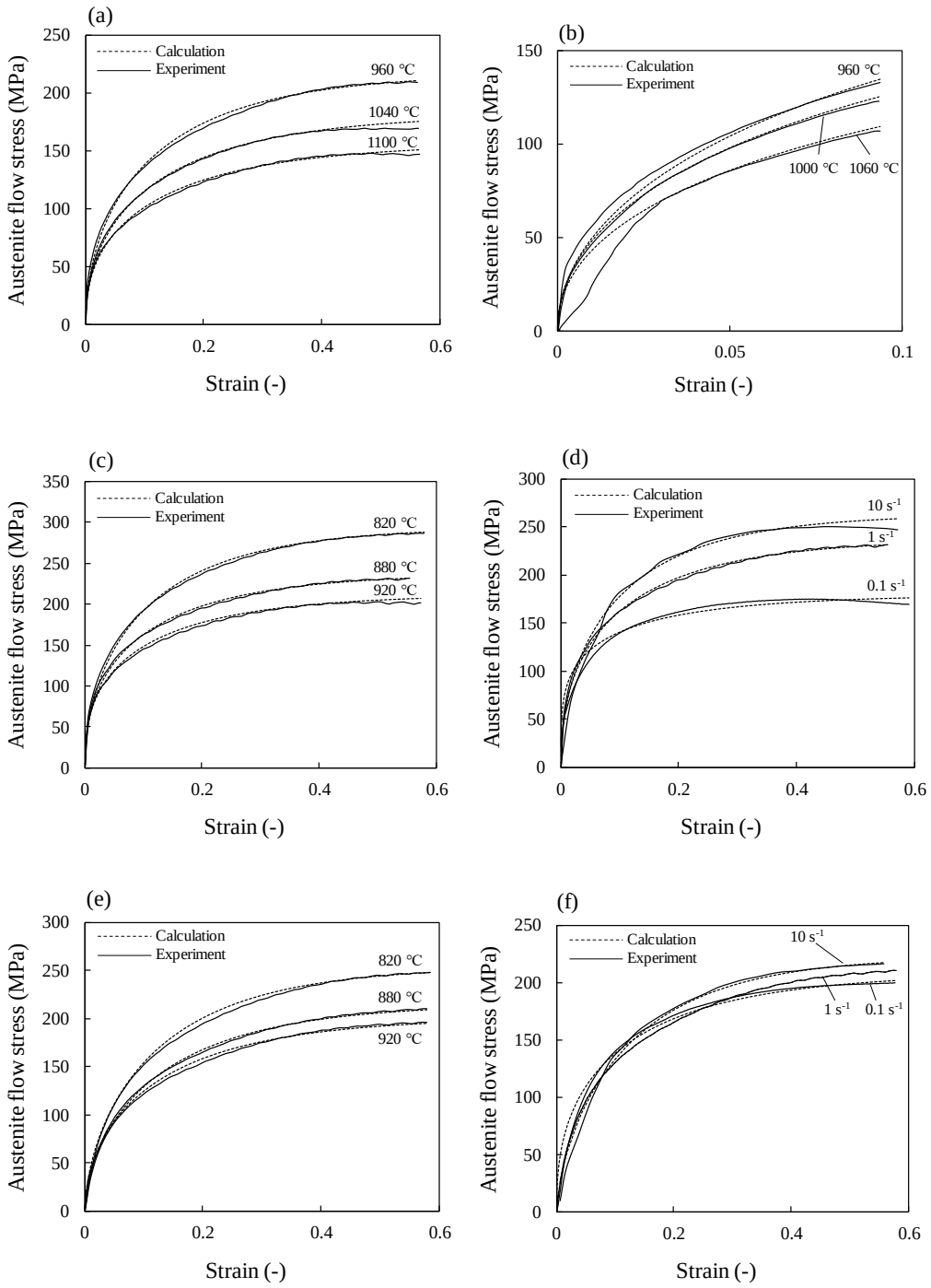

Fig. 5.1 Stress–strain curves in of (a) Fe–Mo–C system at strain rate of 1 s^{-1} and strain range from 0 to 0.6, (b) Fe–Mo–C system at strain rate of1 s^{-1} and strain range from 0 to 0.1, (c) Steel A at strain rete of 1 s^{-1}, (d) Steel A at temperature of 880°C, (e) Steel B at strain rete of 1 s^{-1}, (f) Steel B at temperature of 880°C.

Table 5.1 Value of the parameter *a* and *n* in equation (3.9).

	Temperature (°C)	strain rate (s^{-1})	*a*	*n*
Fe–Mo–C	960	1	1.45	0.8
	1000	1	1.45	0.8
	1040	1	1.45	0.8
	1060	1	1.45	0.8
	1100	1	1.39	0.85
Steel A	820	1	1.7	0.9
	880	0.1	1.5	1.5
		1	1.55	0.95
		10	1.38	1.1
	920	1	1.5	1.1
Steel B	820	1	1.52	0.75
	880	0.1	1.8	0.9
		1	1.45	0.7
		10	1.2	0.8
	920	1	1.46	0.75

5.1.2. Internal back stress

The internal back stress was calculated using equation (3.15). Here, *M* is the average Taylor factor of 3 (Kocks & Mecking 2003), α is a numerical constant of 0.15 (Estrin 1996), *b* is the magnitude of the dislocation Burgers vector of 0.258 nm (Frost & Ashby 1982), *k* is a constant of 2, and *G* is the shear modulus given by:

$$\boldsymbol{G = G_0\left(1 + \frac{T - 300}{T_M}\right)\frac{T_M}{\mu_0}\frac{\mathrm{d}\mu}{\mathrm{d}T}}, \tag{5.1}$$

$$\boldsymbol{\frac{T_M}{\mu_0}\frac{\mathrm{d}\mu}{\mathrm{d}T} = -0.91 \ \ (\mathbf{for}\ \gamma - \mathbf{iron})}, \tag{5.2}$$

where G_0 is the shear modulus at 300 K of 81 GPa, T_M is melting temperature of 1810 K (Frost & Ashby 1982).

5.1.3. Chemical opposing force

The chemical opposing force was calculated using the *Thermocalc* software with the TCFE6 data–base as shown in **Fig. 5.2**. The results from *Thermocalc* were fitted by a quadratic approximation. The fitting parameters of the quadratic approximation are listed in **Table 5.2**.

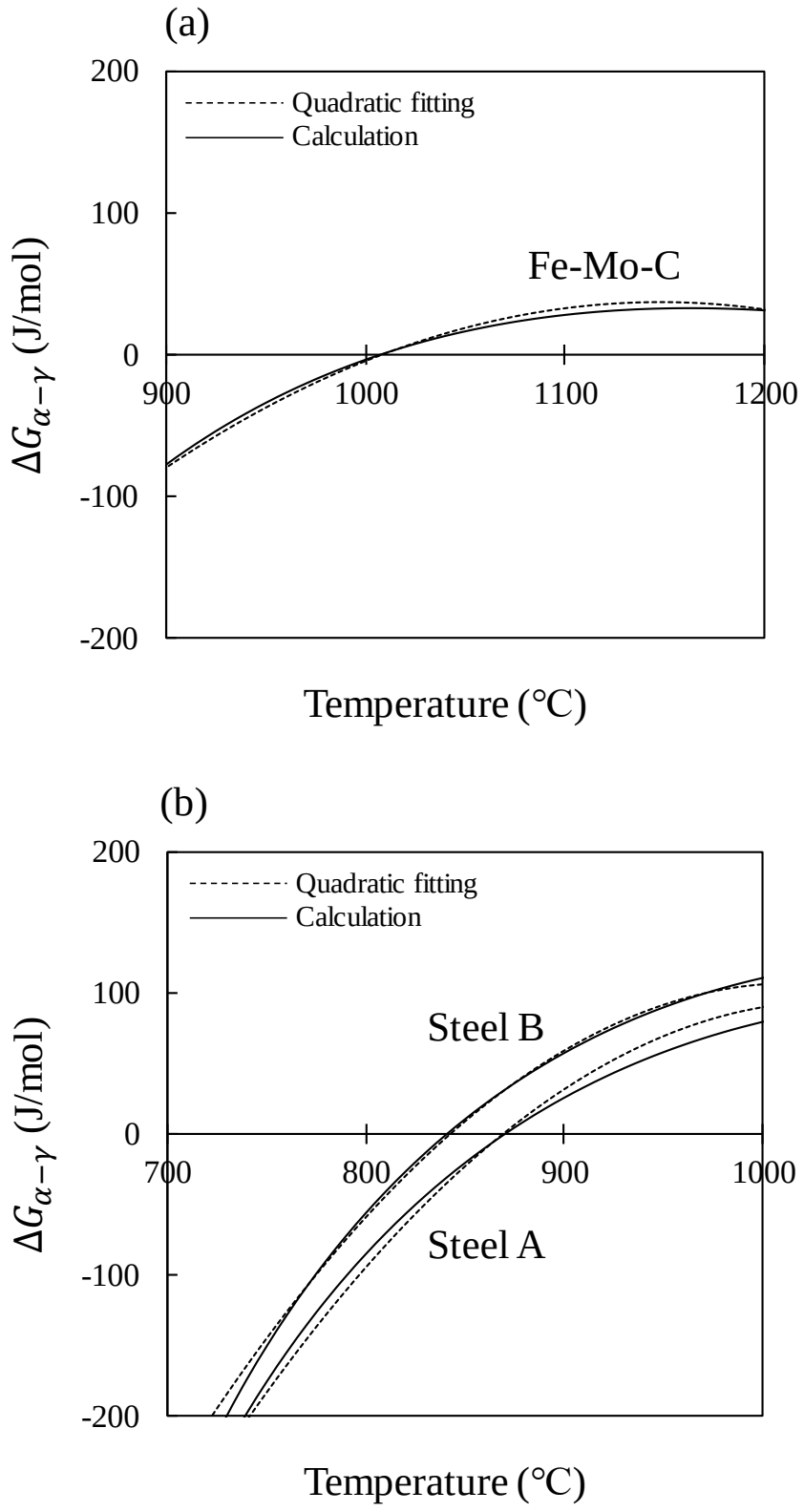

Fig. 5.2 Chemical Gibbs energy difference between austenite and ferrite of (a) Fe–2.4 wt% Mo–0.1 wt% C and (b) commercial steels from US Steel Canada.

Table 5.2 Fitting parameters for the quadratic equation of $\Delta \mathbf{G}_{\alpha-\gamma} = \boldsymbol{aT^2 + bT + c}$. Here *T* is the absolute temperature.

Steel	*a*	*b*	*c*
Fe–Mo–C	−0.0019	5.4	−3800
Steel A	−0.0034	8.9	−5730
Steel B	−0.00356	9.18	−5808

5.1.4. Critical condition for the dynamic transformation

The dependence of the driving force on strain that was described in section 5.1.1 and 5.1.2 on strain can be seen in **Fig. 5.3**. Here, for the equation (3.1), the Schmid factor m is 0.3, the magnitude of the Burgers vector b is 0.275 nm, and the mean free distance of mobile dislocations L is 1 nm. The point of intersection of the driving force (blue line) and the opposing force (red line) indicates the minimum strain at which the dynamic transformation can take place. As the driving force increases, the intersection shifts to the left side of the figure, which means that the dynamic transformation could happen at lower strains. On the other hand, as the opposing force increases, the intersection moves to right, representing a higher minimum strain. Therefore, in order for the ferrite precipitation to occur there needs to be much more deformation.

Fig. 5.4 and **Fig. 5.5** show the critical temperature, which is the maximum temperature at which the dynamic transformation occurs, as a function of strain, for the

Fe–Mo–C and Fe–C–Mn–Si systems that were outlined previously in **Table 3.1**. As shown by the solid lines in **Fig. 5.4**, at temperatures below 1150°C, the critical temperature increases when strain and strain rate increases. When the strain and strain rate are constant, the dynamic transformation could not happen above the critical temperature. However, as the deformation temperature increases above 1150°C by the broken lines, the critical strain, which is the minimum strain at which the dynamic transformation occurs, decreases. This means that the dynamic transformation will happen again. This ferrite is delta ferrite. This delta ferrite forms because as the deformation temperature increases above the broken line, the chemical Gibbs energy between ferrite and austenite decreases again, as shown in **Fig. 5.2a**.

The critical temperature for Fe–C–Mn–Si system is illustrated in **Fig. 5.5** and **Fig. 5.6**. As the strain and strain rate increases, the critical temperatures of both steel A and B increase. Furthermore, these figures suggest that steel A tends to have a higher critical temperature than steel B. This results suggest that steel A can more easily undergo the dynamic transformation to ferrite than steel B.

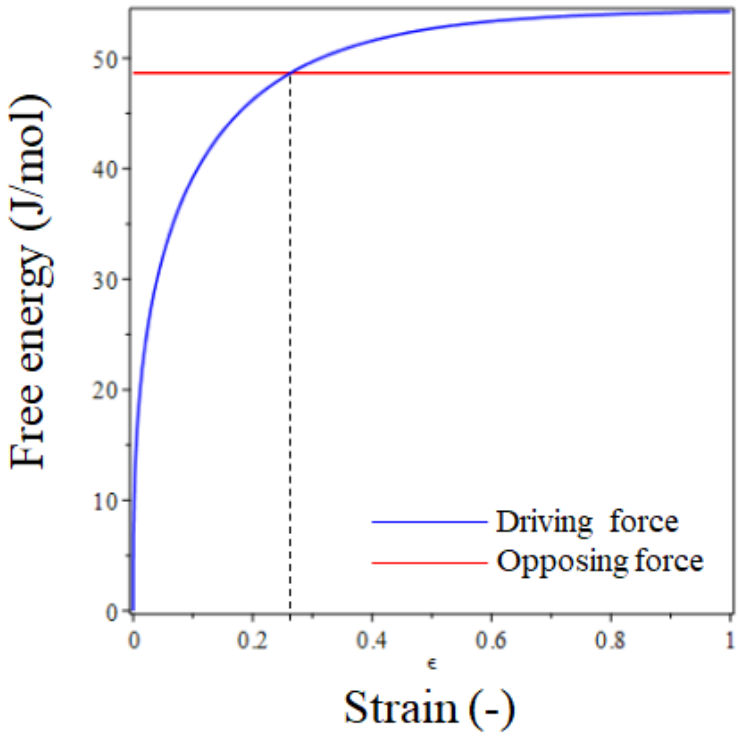

Fig. 5.3 Comparison of the driving force and the opposing force as functions of strain.

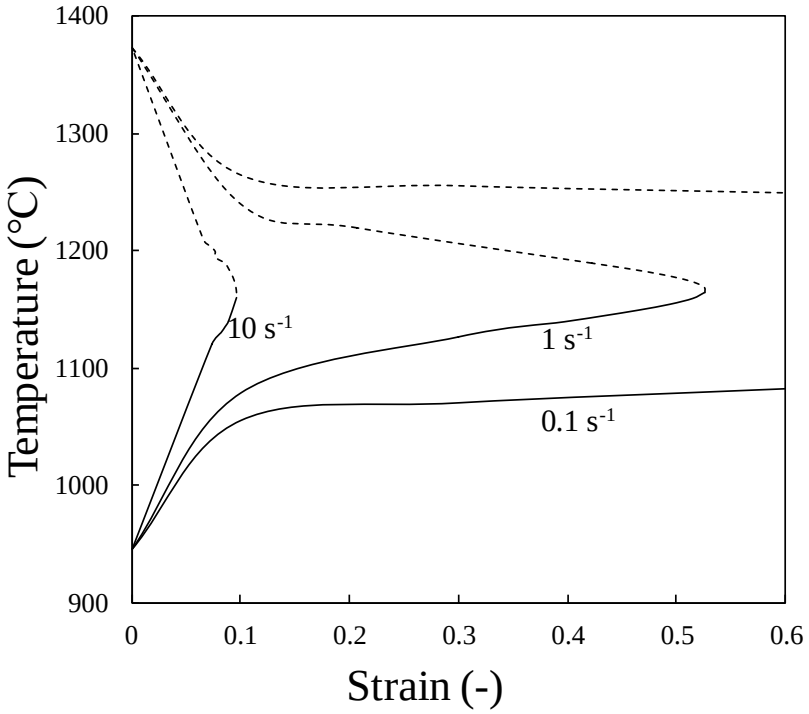

Fig. 5.4 Comparison of the critical temperature for the dynamic transformation as a function of strain of the Fe–Mo–C system at strain rates ranging from 0.1 s^{-1} to 10 s^{-1}.

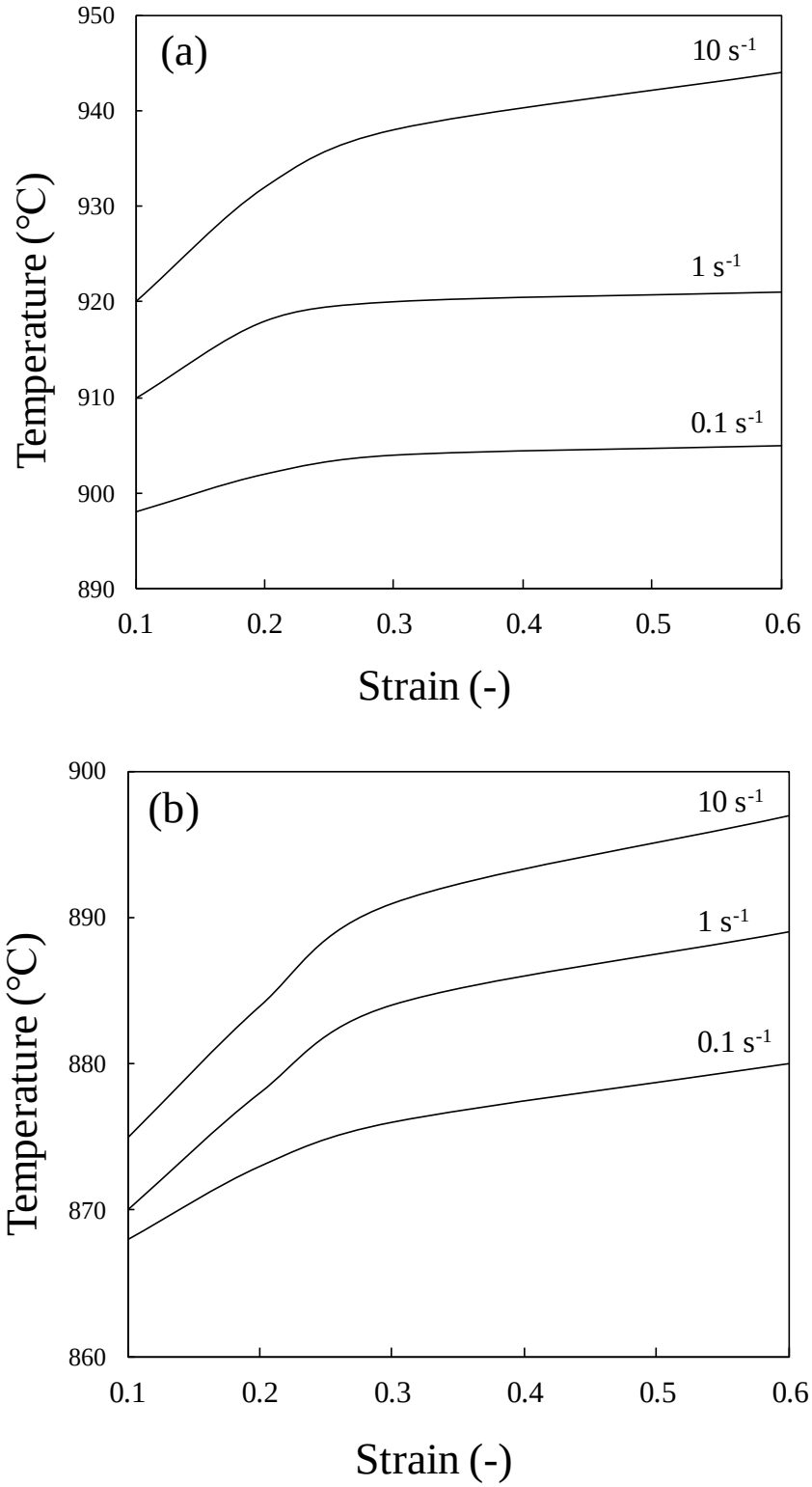

Fig. 5.5 Comparison of the critical temperature for the dynamic transformation as a function of strain at strain rates ranging from 0.1 s^{-1} to 10 s^{-1} of (a) Steel A and (b) Steel B.

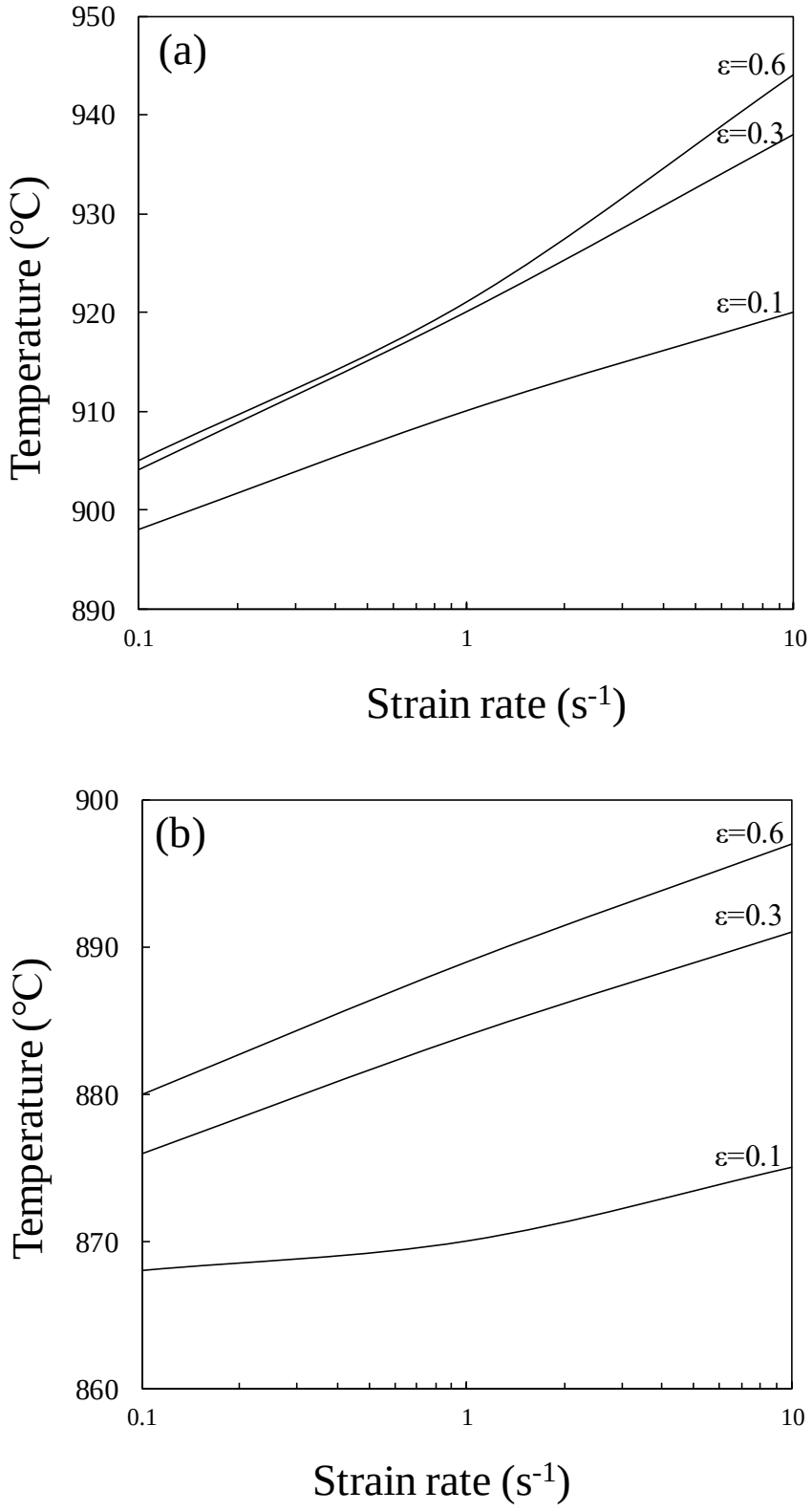

Fig. 5.6 Comparison of the critical temperature for the dynamic transformation as a function of strain rate at strain ranging from 0.1 to 0.6 of (a) Steel A and (b) Steel B.

5.2 Dilatometry experiment

The dilatometry experiment was carried out in order to observe the reverse transformation from ferrite to austenite by measuring the length change during isothermal holding time. As shown in **Fig. 5.7**, the experimental conditions were distributed several temperature, strain, and strain rate. Solid lines indicate the critical temperature from the model calculation, and two broken lines are ortho equilibrium temperature and para equilibrium temperature, respectively.

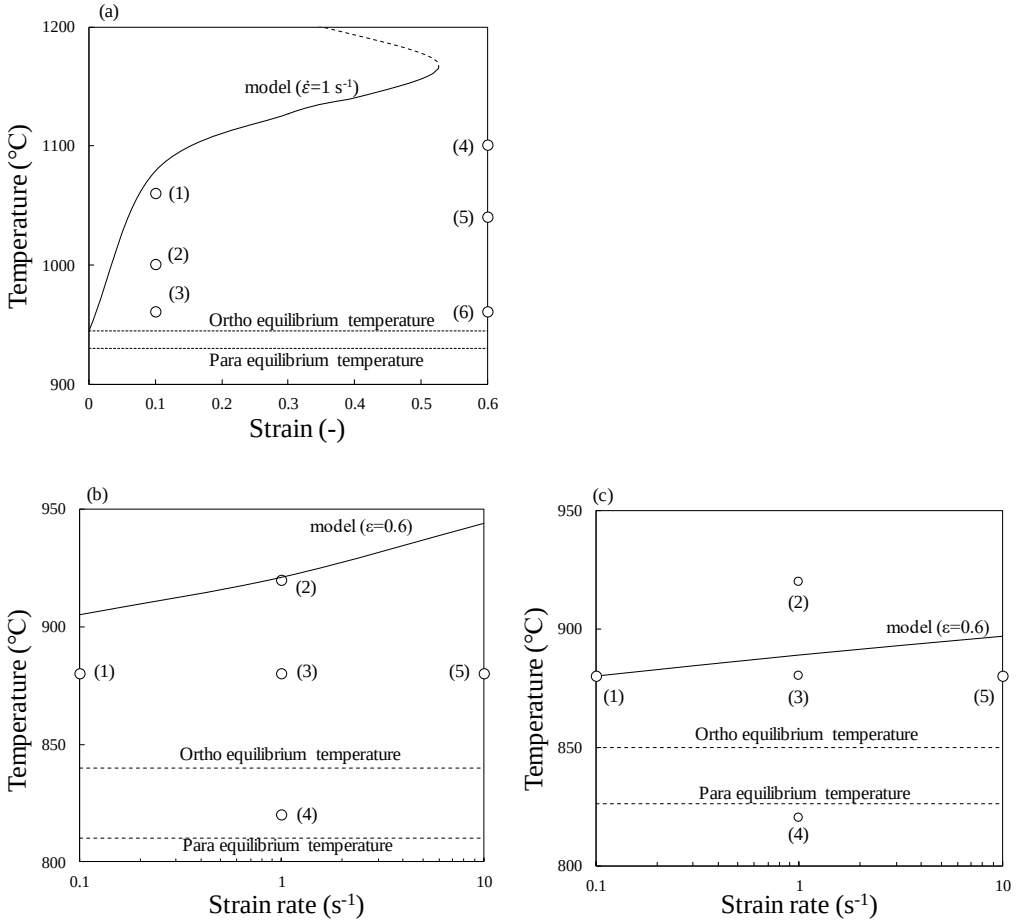

Fig. 5.7 Experimental conditions at (a)Fe–Mo–C system, (b)Steel A (Fe–C–Mn–0.9 wt% Si), and (c)Steel B (Fe–C–Mn–0.5 wt% Si).

5.2.1.Dilatometry curves

The dilatometry curves for various combinations of temperature, strain, and strain rate are shown in **Fig. 5.8** to **Fig. 5.15**. The length change is adjusted to start at 0 μm.

As can be seen in **Fig. 5.8**, at the beginning of the holding time, the length first increases and then peaks after holding for around 1 s. For the samples that were held at 1040°C and 1100°C, after the peak, it can be seen that the length subsequently decreases

until the end of the holding period. However, for the sample held at 960°C, it can be seen that after an initial reduction in length, the length gradually increases after 1 s. The total reduction in length is higher when the temperature is higher.

As shown in **Fig. 5.9**, for the case with a strain of 0.1, after two seconds the length change is almost constant at each temperature. These plots show expansion from the starting point.

From **Fig. 5.10**, which shows length change curves for Steel A samples, it can be seen that the length also peaks around 1 second. For the sample held at 920°C, the length gradually increases after 2 seconds, similar to the behavior seen in **Fig. 5.8**. The length contraction clearly depends on the temperature. Even though the signal stops after 5 seconds for the sample held at 920°C, the trend of this series after 2 seconds does not decrease, and thus the lack of data at larger times is not important. **Fig. 5.11**, which highlights dilatometry experiments on Steel B, suggests that the highest sample contraction is for the sample held at 880°C. For the sample held at 820 °C, the length slowly increases after 2 seconds as well.

According to **Fig. 5.12** and **Fig. 5.13**, it is clear that the length contraction depends on the strain. Also, by comparing **Fig. 5.12** and **Fig. 5.13**, it is apparent that the magnitude of the contraction and expansion for Steel B is bigger than that of Steel A.

Fig. 5.14 and **Fig. 5.15** explore the effect of strain rate for Steel A and Steel B respectively and show similar behavior for both steels. Based on these figures it appears that the length contraction does not depend on strain rate.

All of the data in **Fig. 5.8** to **Fig. 5.15** have peaks that occur during the initial second. Thus, it can be suggested that the maximum amount of the dynamic transformation ferrite exists at this point. Conversely, the minimum point on these plots represents the point where all of the ferrite finishes its re–transformation to austenite. Therefore, in order to calculate the volume fraction of ferrite after deformation, the length change between the peak and the minimum points needs to be calculated.

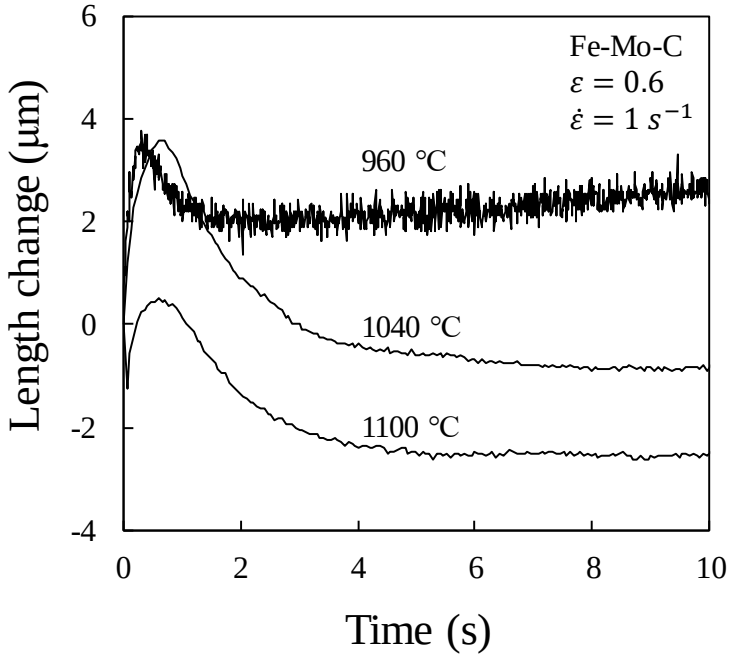

Fig. 5.8 Length change during isothermal holding time of Fe–Mo–C system at a strain

of 0.6, strain rate of 1 s^{-1}, and various temperatures.

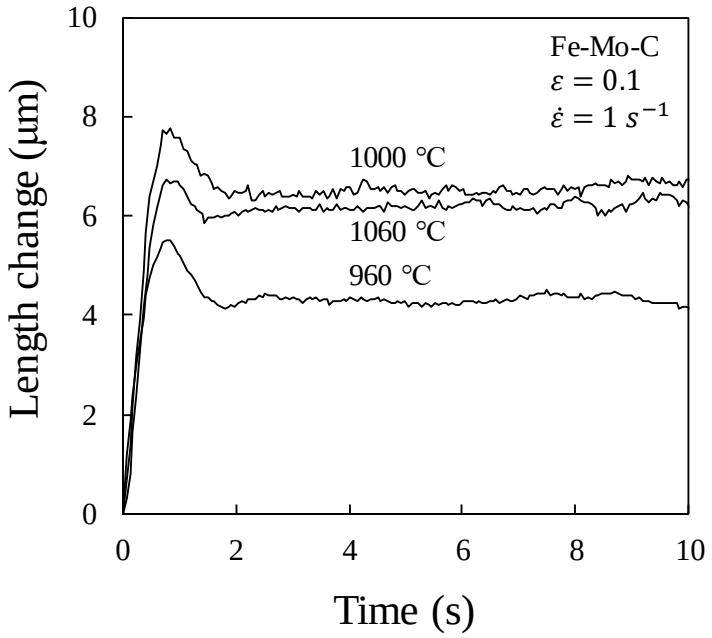

Fig. 5.9 Length change during isothermal holding time of Fe–Mo–C system at a strain of 0.1, strain rate of 1 s^{-1}, and various temperatures.

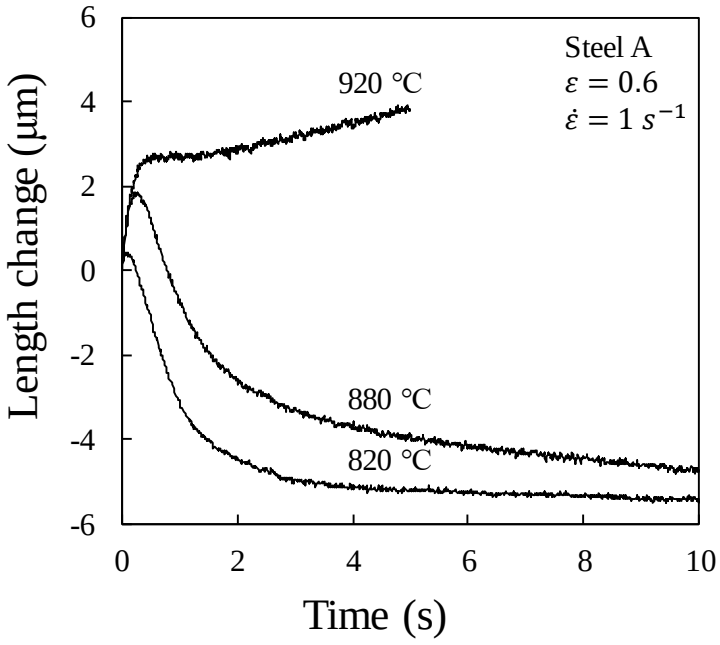

Fig. 5.10 Length change during isothermal holding time of Steel A at a strain of 0.6,

strain rate of 1 s^{-1}, and various temperatures.

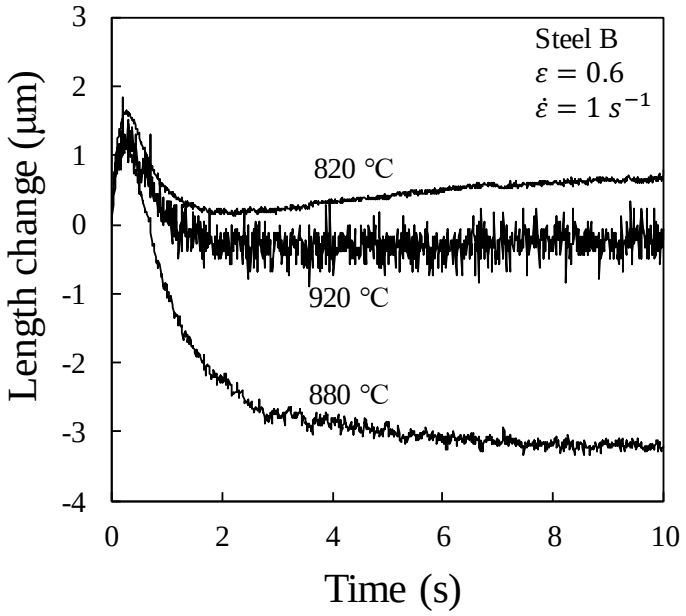

Fig. 5.11 Length change during isothermal holding time of steel B at a strain of 0.6, strain rate of 1 s^{-1}, and various temperatures.

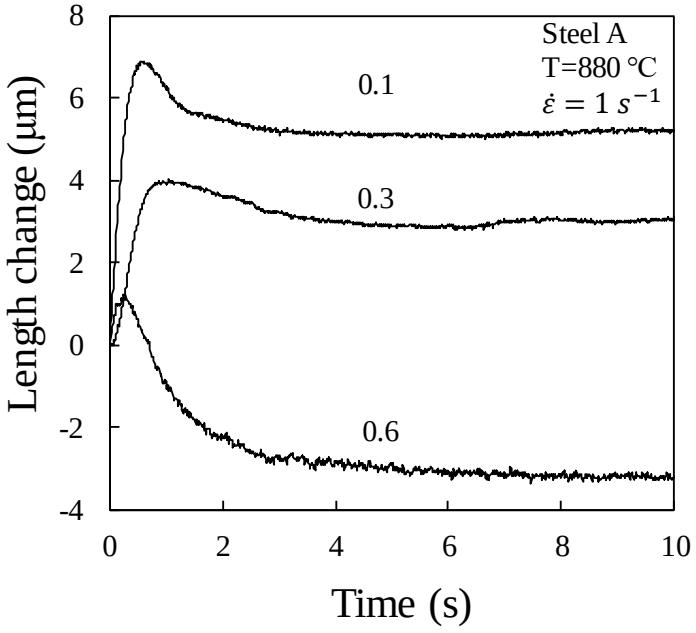

Fig. 5.12 Length change during isothermal holding time of Steel A at a temperature of 880°C, strain rate of 1 s^{-1}, and several strains.

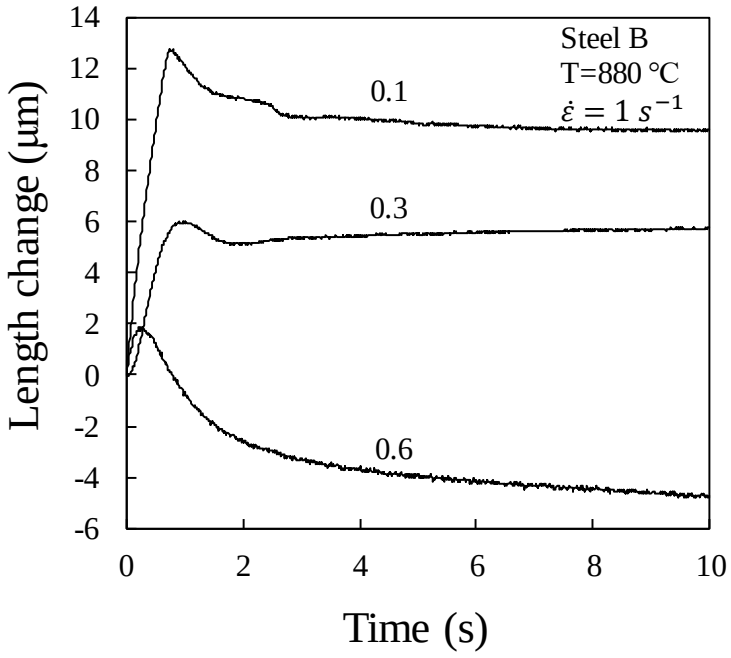

Fig. 5.13 Length change during isothermal holding time of Steel B at a temperature of 880°C, strain rate of 1 s^{-1}, and several strains.

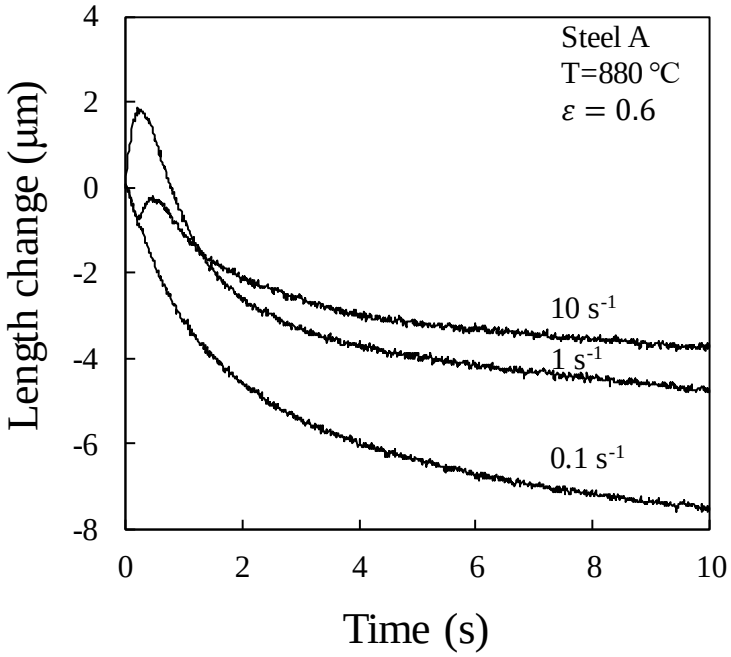

Fig. 5.14 Length change during isothermal holding time of Steel A at a temperature of 880°C, strain of 0.6, and several strain rates.

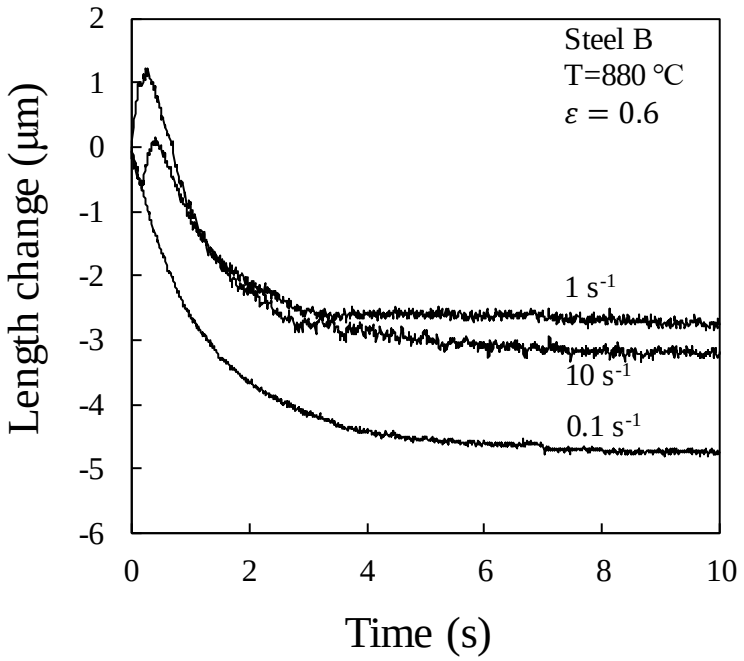

Fig. 5.15 Length change during isothermal holding time of Steel B at a temperature of 880°C, strain of 0.6, and several strain rates.

5.2.2. Temperature effect on dilatation

As shown in **Fig. 5.16**, the compression testing was accompanied by a temperature change because of processing heating. Though the induction heater was controlled by feedback controlling based on a thermocouple's temperature, the thermal controller needs over two seconds to follow the goal temperature. Consequently, the original dilatation curve was affected by temperature change during the first 0.5 seconds. To solve this problem, temperature correction was applied to the dilatation data. The thermal expansion L_{heat} is given by:

$$\boldsymbol{L_{heat} = (T - T_{aim})\alpha L_{def}}, \tag{5.3}$$

where T_{aim} is the goal temperature, α is the coefficient of thermal expansion, and L_{def} is the sample length after deformation. α was obtained by monitoring the length change of sample while cooling it from 1200°C to the deformation temperature as shown in **Fig. 5.17**. The values of thermal expansion coefficient, α, for the Fe–Mo–C system, Steel A, and Steel B were found to be 2.67×10^{-5} /°C, 2.49×10^{-5} /°C, and 2.72×10^{-5} /°C, respectively.

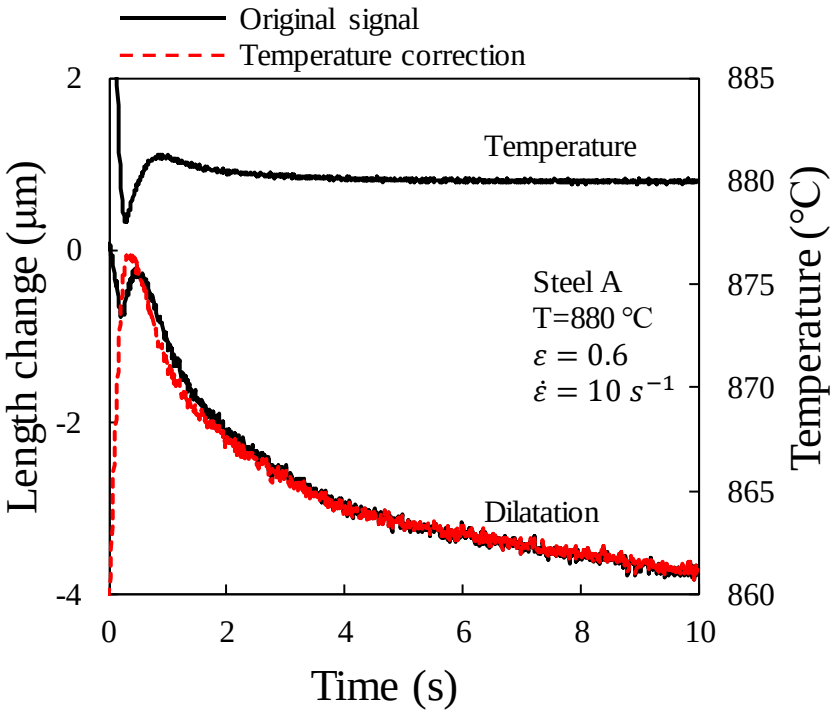

Fig. 5.16 Temperature correction on the dilatation curve for Steel A at a temperature of 880°C, strain of 0.6, and strain rate of $10s^{-1}$.

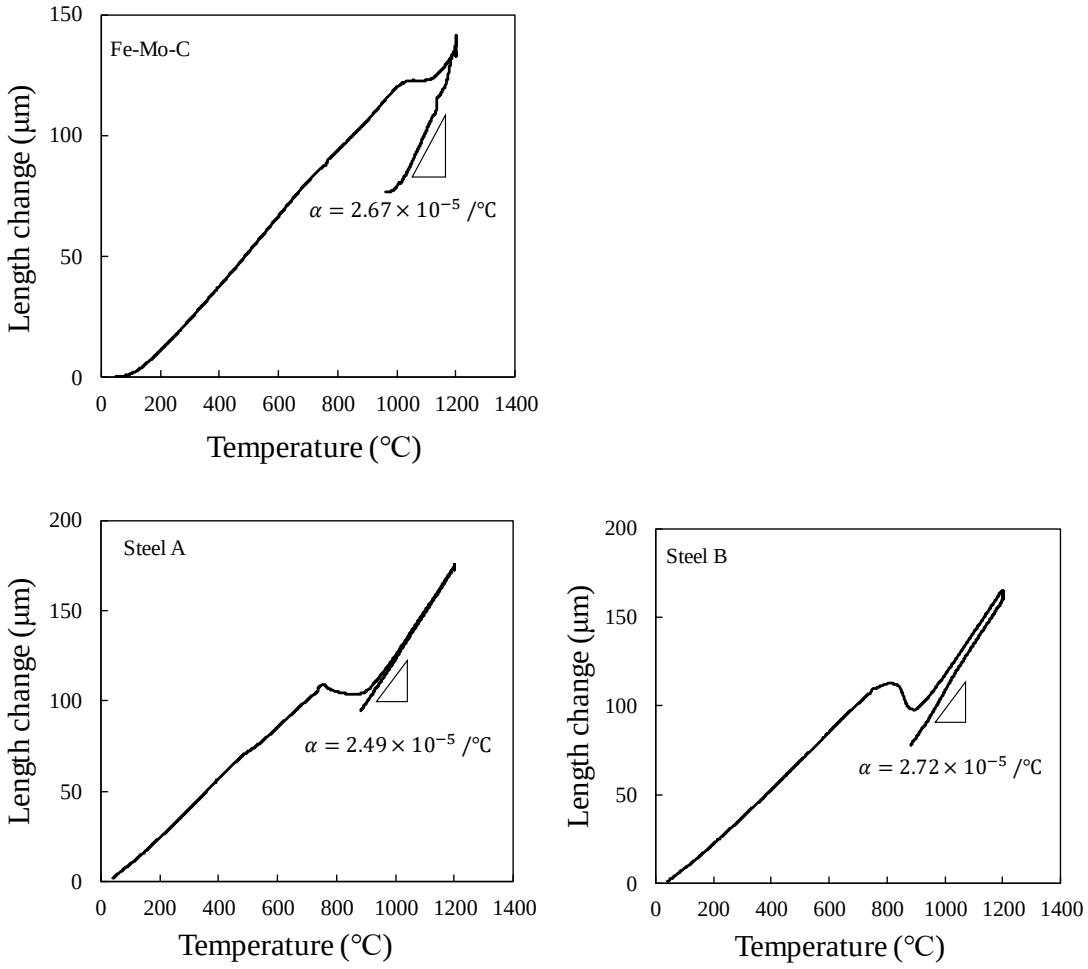

Fig. 5.17 Plots of length change vs. temperature used to determine the coefficient of thermal expansion from the experiments.

5.2.3. Conversion from length data to volume fraction of ferrite

The length data needs to be converted to volume fraction of ferrite in order to compare to the results of the metallography. The length difference between 100% ferrite and 100% austenite as a function of deformation temperature is shown in **Fig. 5.18**, with Δl_α and Δl_γ representing the ferrite and austenite length changes at the deformation

temperature after the linear interpolation of the experimental data. If a full ferrite specimen transforms to full austenite, the length ratio R_1 between ferrite and austenite is also described as:

$$\mathbf{R_1} = \frac{\boldsymbol{l_0 + \Delta l_\gamma}}{\boldsymbol{l_0 + \Delta l_\alpha}}, \tag{5.4}$$

where l_0 is the initial length of a specimen before heating.

A schematic diagram of the method for converting from length change to the volume fraction of ferrite, V_α, is shown in **Fig. 5.19**. In this diagram, ferrite and austenite are separated in order to make it easier to understand. The length for the dynamic transformation ferrite after deformation can be represented as $L_{deform}V_\alpha$. If this ferrite transforms to austenite completely, the length of austenite is described as $L_{hold} - L_{deform}(1 - V_\alpha)$. The length ratio R_2 between the ferrite and re–transformed austenite can be written as:

$$\mathbf{R_2} = \frac{\boldsymbol{L_{hold} - L_{deform}(1 - V_\alpha)}}{\boldsymbol{L_{deform}V_\alpha}}. \tag{5.5}$$

These two length ratio are the same and can be equated as follows:

$$\frac{L_{hold} - L_{deform}(1 - V_\alpha)}{L_{deform} V_\alpha} = \frac{l_0 + \Delta l_\gamma}{l_0 + \Delta l_\alpha}. \quad (5.6)$$

Equation (5.6) can be transformed as:

$$V_\alpha = \frac{L_{deform} - L_{hold}}{L_{deform}\left(1 - \frac{l_0 + \Delta l_\gamma}{l_0 + \Delta l_\alpha}\right)}. \quad (5.7)$$

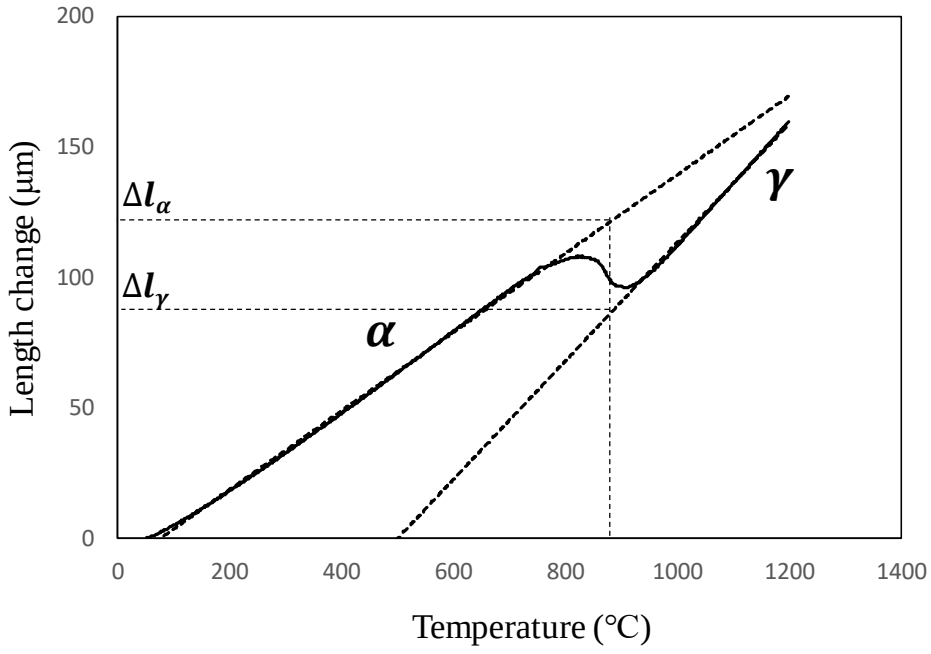

Fig. 5.18 Length difference between full ferrite and full austenite specimen as a function of temperatures.

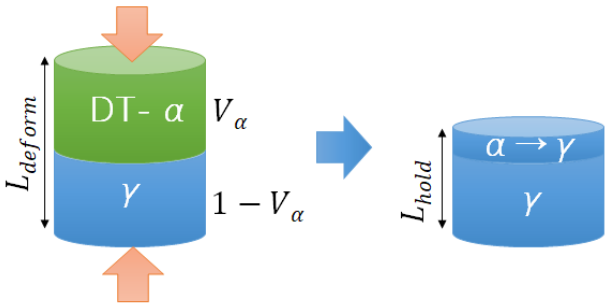

Fig. 5.19 Schematic diagram of the reverse transformation.

Fig. 5.20 to **Fig. 5.23** illustrates the calculated volume fraction of the dynamic transformation ferrite using equation (5. 9).

Fig. 5.20 to **Fig. 5.22** shows that more dynamic transformation ferrite can be generated for the higher silicon alloy (Steel A) in overall trend. Also, when the level of strain increases, the volume fraction of ferrite increases. As can be seen in **Fig. 5.21**, the amount of ferrite reach a maximum at intermediate temperatures. Also, at highest temperature, the more ferrite fraction generates at lower silicon steel. It can be seen in the **Fig. 5.22** that the ferrite fraction increases between 0.1 and 1 s^{-1}, and decreases between 1 and 10 s^{-1}. As can be seen in **Fig. 5.23** for the Fe–Mo–C system, the amount of ferrite precipitation at a strain of 0.6 is clearly higher than at a strain of 0.1. Also, it can be seen that at lower temperatures the ferrite fraction increases as temperature increases. However, at higher temperatures, the amount of ferrite is constant or decreases with increasing temperatures.

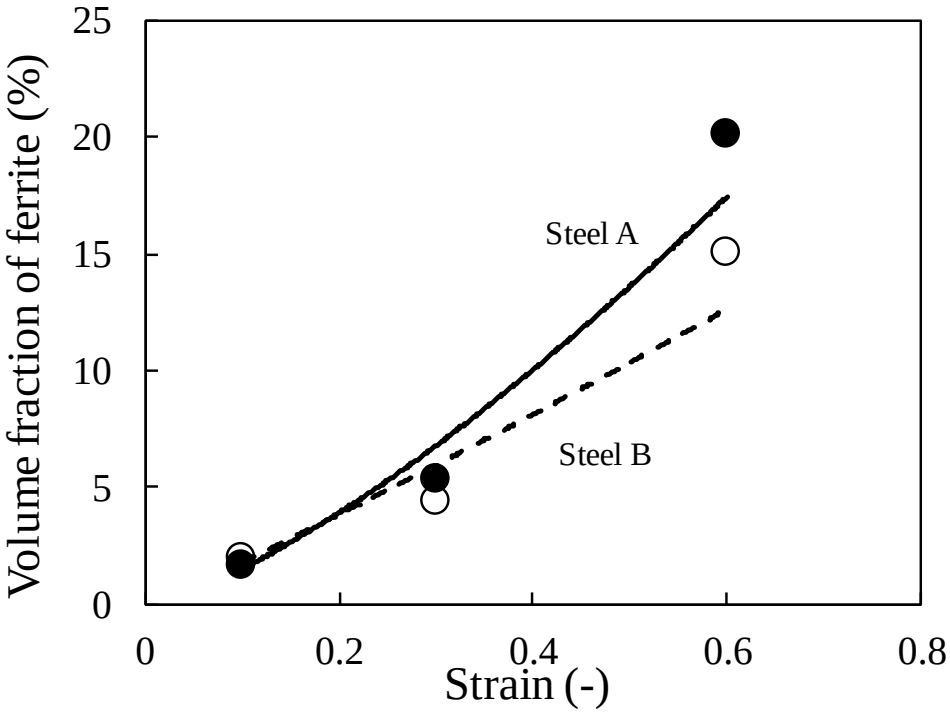

Fig. 5.20 Volume fraction of ferrite at different strain levels for commercial steels.

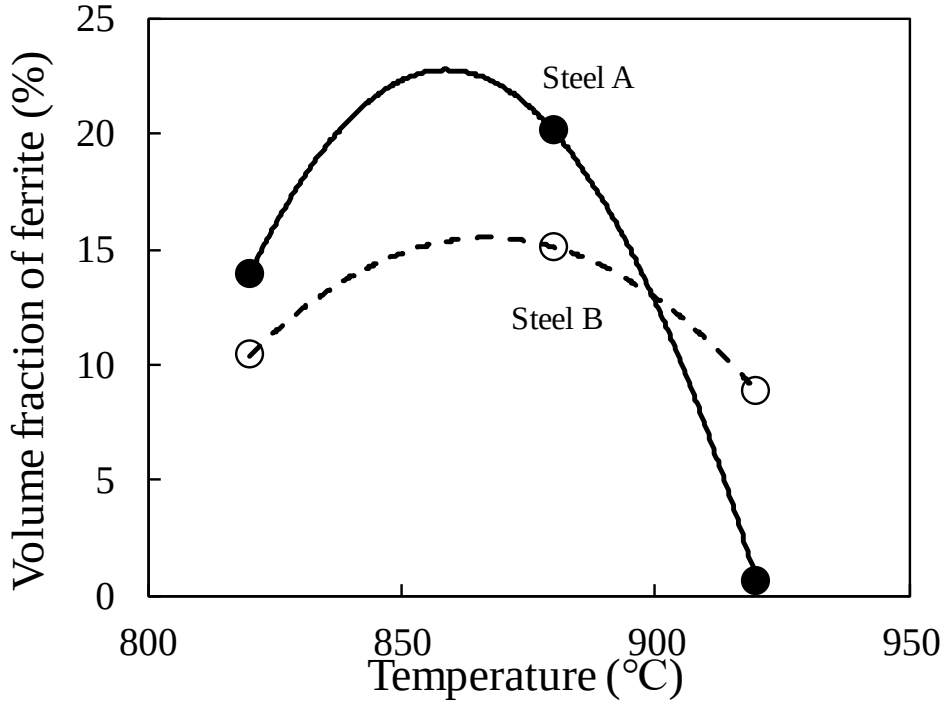

Fig. 5.21 Volume fraction of ferrite at different temperatures for commercial steels.

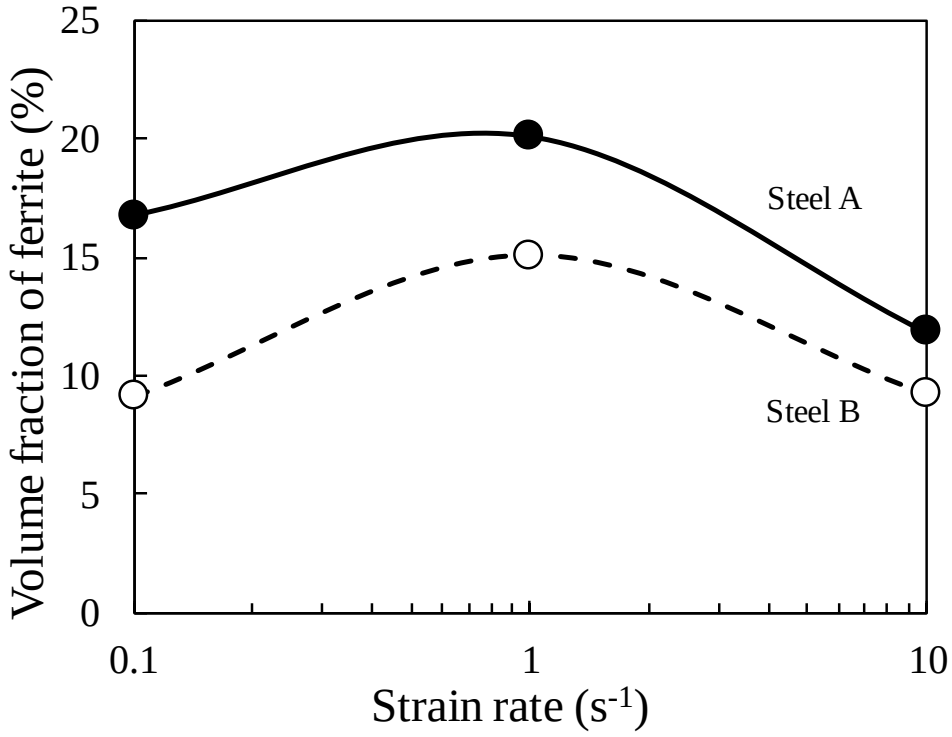

Fig. 5.22 Volume fraction of ferrite at different strain rates for commercial steels.

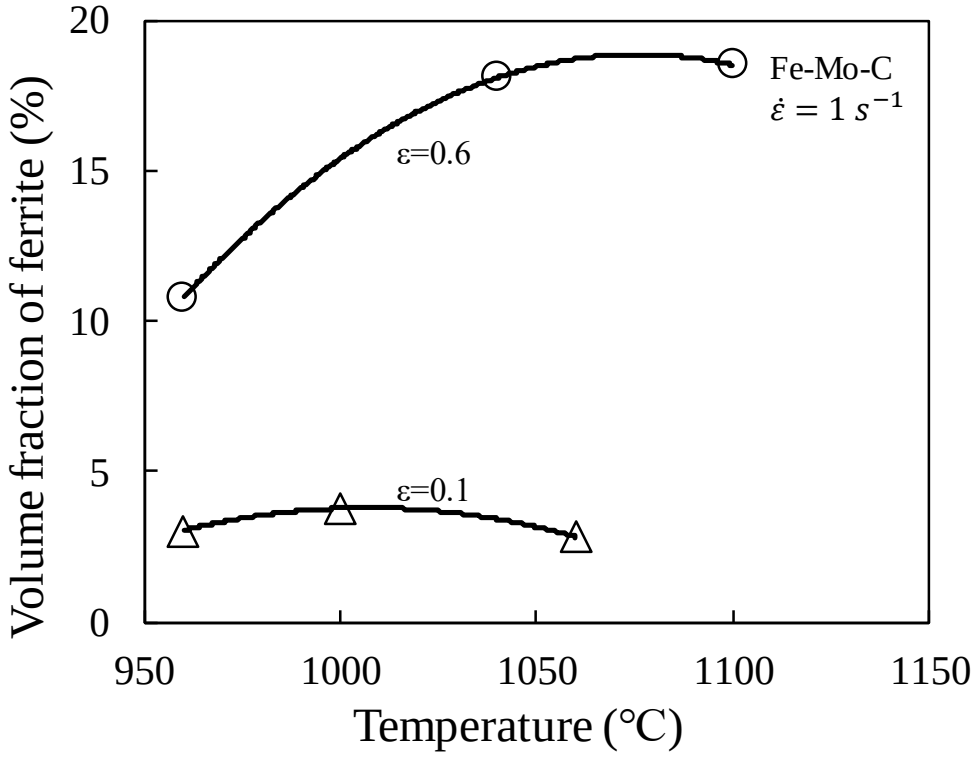

Fig. 5.23 Volume fraction of ferrite at different temperatures for the Fe–Mo–C system.

5.2.4. Microstructure observation

The optical metallography for the Fe–Mo–C system is shown in **Fig. 5.24**. In **Fig. 5.24a** for a sample held at 1060°C and a strain of 0.1, it can be seen that the microstructure is almost martensitic with some polygonal ferrite in the prior austenite grain boundaries. The amount of ferrite present is only 6.1%. At a lower temperature and the same strain level, the volume fraction of ferrite increases to 13.1% as shown in **Fig. 5.24b**. On the other hand, as can be seen in **Fig. 5.24c**, more ferrite precipitates when a higher strain of 0.6 is applied. Furthermore, at higher temperatures, the volume fraction of ferrite is shown to reach up to 67.3%.

EBSD images for the sample held at 960°C and strained to 0.6 are illustrated in **Fig. 5.25**. As can be seen in **Fig. 5.25a**, polygonal ferrite is distributed in prior austenite grain boundaries. The grain size of the ferrite is five to ten microns. It can be seen in **Fig. 5.25b** that Widmanstätten ferrite is shown near the prior austenite grain boundaries.

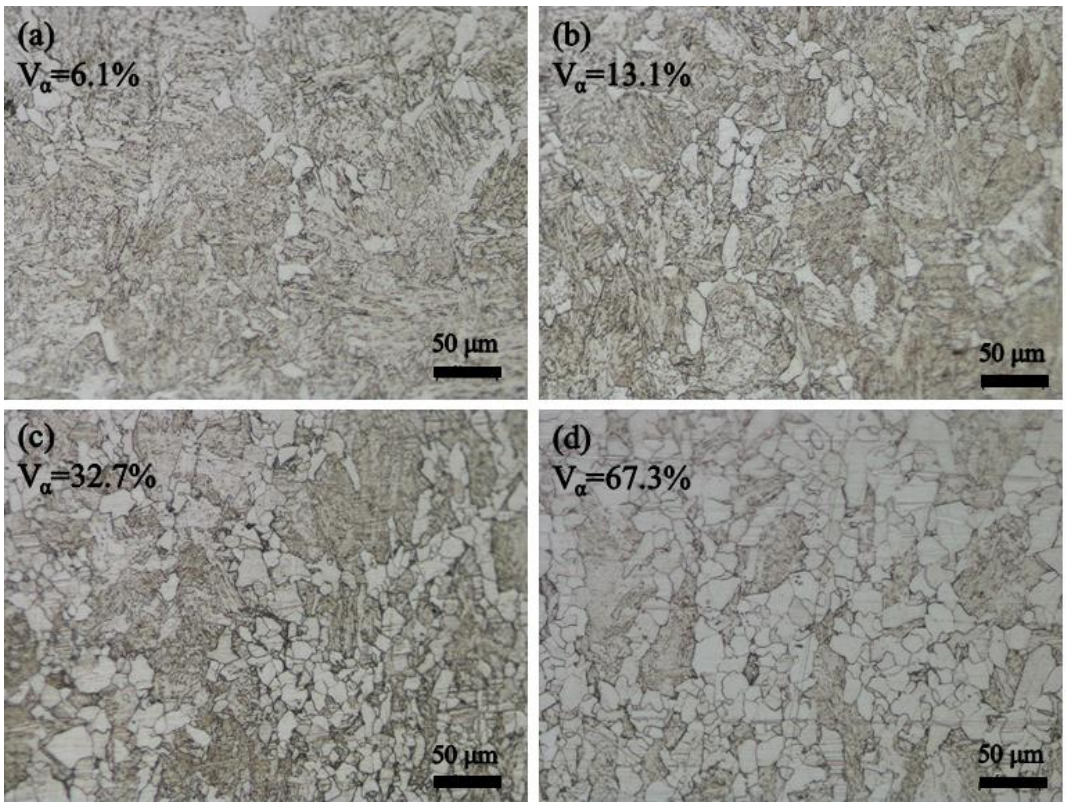

Fig. 5.24 Optical microscopy image of Fe–Mo–C system at (a) 1060°C, ε=0.1, (b) 1000°C, ε=0.1, (c) 1100°C, ε=0.6, and (d)1040°C, ε=0.6. V_α means the volume fraction of ferrite.

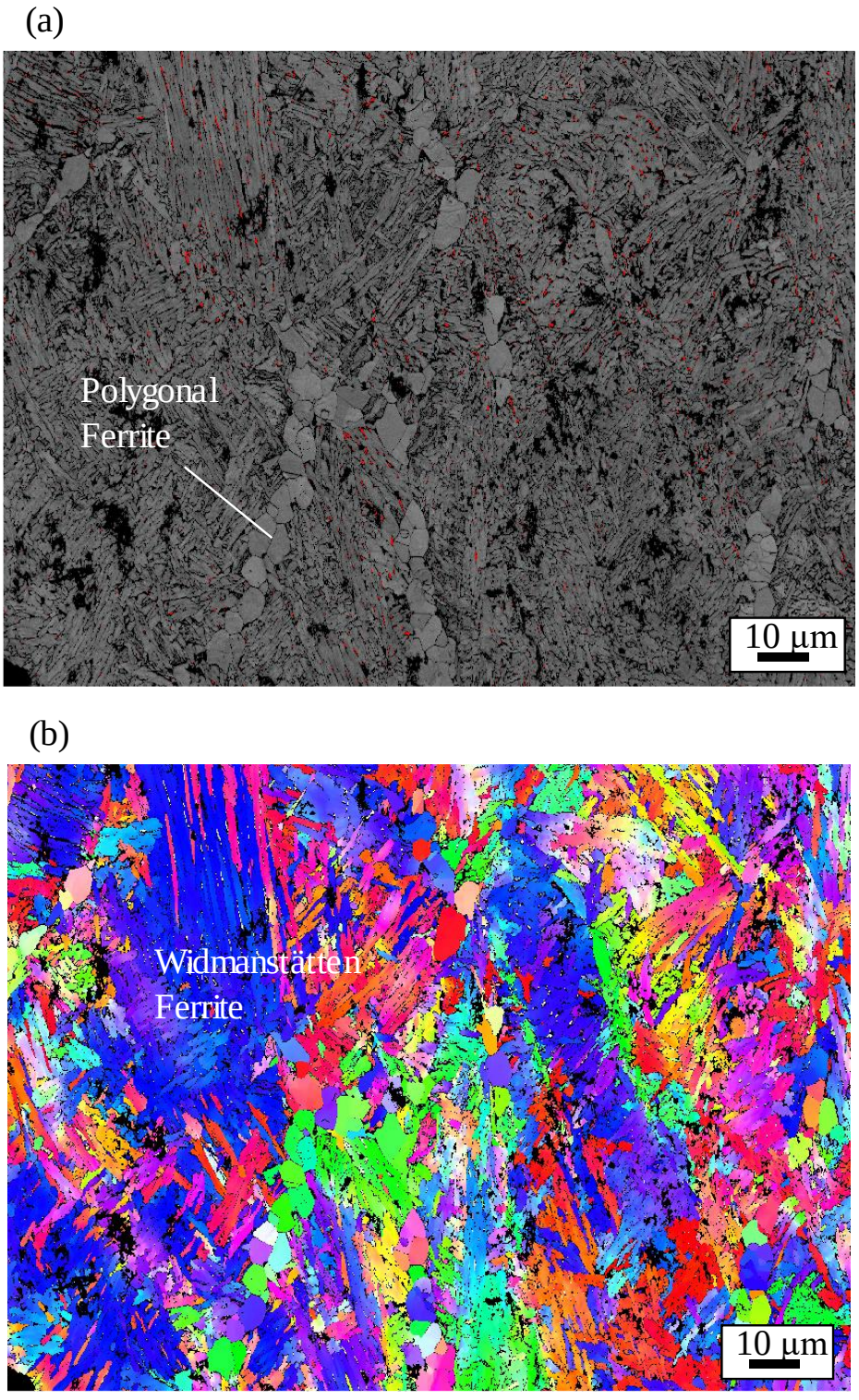

Fig. 5.25 EBSD micrograph at 960 °C and ε=0.6 (a)band contrast image, and (b) IPF map.

Chapter 6. Discussions

In this chapter, the characteristics of the dynamic transformation which were obtained from the model calculation and the experimental results are discussed.

6.1 Fe–Mo–C system

6.1.1. Comparison of the dilatometry results and the metallography

As can be seen in **Table 6.1**, the ferrite fraction is quite different between the dilatometer and optical metallography results. The ferrite fraction from the optical metallography is counted based on the polygonal ferrite present, as shown in **Fig. 5.24**. However, Jonas et al. discovered that the dynamic transformation is displacive transformation and thus forms Widmanstätten ferrite (Jonas & Ghosh 2013). Therefore, as can be seen in **Fig. 5.24**, the higher levels of polygonal ferrite transforms from the austenite during quenching because the steel in this Fe–Mo–C system does not have enough hardenability.

An IPF map of EBSD is illustrated in **Fig. 5.25b**, for the condition with a temperature of 960°C, strain of 0.6, and strain rate of 1 s^{-1}. In this map the Widmanstätten structure can be still observed, and this Widmanstätten ferrite fraction is 9.8 %, which is corresponds well to the ferrite fraction found from the dilatometry

experiment as shown in **Table 6.1(6)**.

Table 6.1 Comparison of the volume fraction of ferrite between the dilatometry experiment and optical microscopy image at Fe–Mo–C system as shown in **Fig. 5.23**–**Fig. 5.25**. These numbers for the dilatometry correspond to **Fig. 5.7a**.

No.	Temperature (°C)	Strain (—)	Dilatometer (%)	Metallography (%)
(1)	1060	0.1	2.8	6.1 (Optical)
(2)	1000	0.1	3.8	13.1 (Optical)
(3)	960	0.1	3.1	–
(4)	1100	0.6	18.5	32.7 (Optical)
(5)	1040	0.6	18.1	67.3 (Optical)
(6)	960	0.6	10.8	9.8 (EBSD)

6.1.2. Validation of the model calculation

The model for ferrite growth as a result of the movement of disconnections under applied stress, which was proposed in Chapter 3, will now be validated. This motion is opposed by the back stress present and by the increases in the Gibbs energy that occur as a result of the deformation of ferrite above Ae3.

As shown in section 5.2.3, and in particular in **Fig. 5.23**, the trend from the dilatometry experiments of increasing volume fractions of ferrite at higher levels of strains corresponds to the model calculation in **Fig. 5.4**. However, in terms of temperature, the ferrite precipitation decreases as temperature decreases even though the Gibbs energy obstacle decreases (see No.5 and 6 in **Table 6.1**). The reason for this

will be discussed in section 6.5.

6.2 Fe–C–Mn–Si system

Commercial steels from US Steel Canada which belong to the Fe–C–Mn–Si system, as shown in **Table 4.1**, were also investigated using the dilatometer to validate the disconnection model.

The volume fraction of ferrite obtained from the dilatometry experiments are plotted in **Fig. 6.1**. Based on the model calculations, the critical temperature of Steel A is higher than that of Steel B, and is represented in these figures by the solid line. This result indicates that higher silicon steels can experience the dynamic transformation more easily. Jonas et al. investigated the dynamic transformation using samples with different silicon compositions, and they concluded that silicon increases the driving force and decreases the Gibbs energy obstacle (Aranas, Jr & Jonas 2015). This suggests that higher silicon steel could generate more dynamic transformation ferrite.

In terms of strain rate, according to **Fig. 6.1a** and **Fig. 6.1b**, the ferrite fraction increases as the strain rate increases from 0.1 to 1 s^{-1}. However, in the range of strain rate from 1 to 10 s^{-1}, the ferrite fraction decreases. The reason for this will be discussed in section 6.4.

In terms of temperature, as shown in **Fig. 6.1a**, the volume fraction of ferrite at the critical temperature of 920°C (see No.2) is only 0.6%, so the model calculation corresponds well to the dilatometry experiment. However, as temperature decreases, the ferrite fraction increases. On the other hand, as shown in **Fig. 6.1b**, the ferrite fraction is 8.8% for the sample above the critical temperature. The reason for this will be discussed in section 6.5.

As temperature drops below the Ae3, the volume fraction of ferrite decreases. This is because our method to observe the dynamic transformation is based on observing the reverse transformation from ferrite to austenite. Therefore, when some ferrite could not transform to austenite, the dilatometry signal could not be obtained.

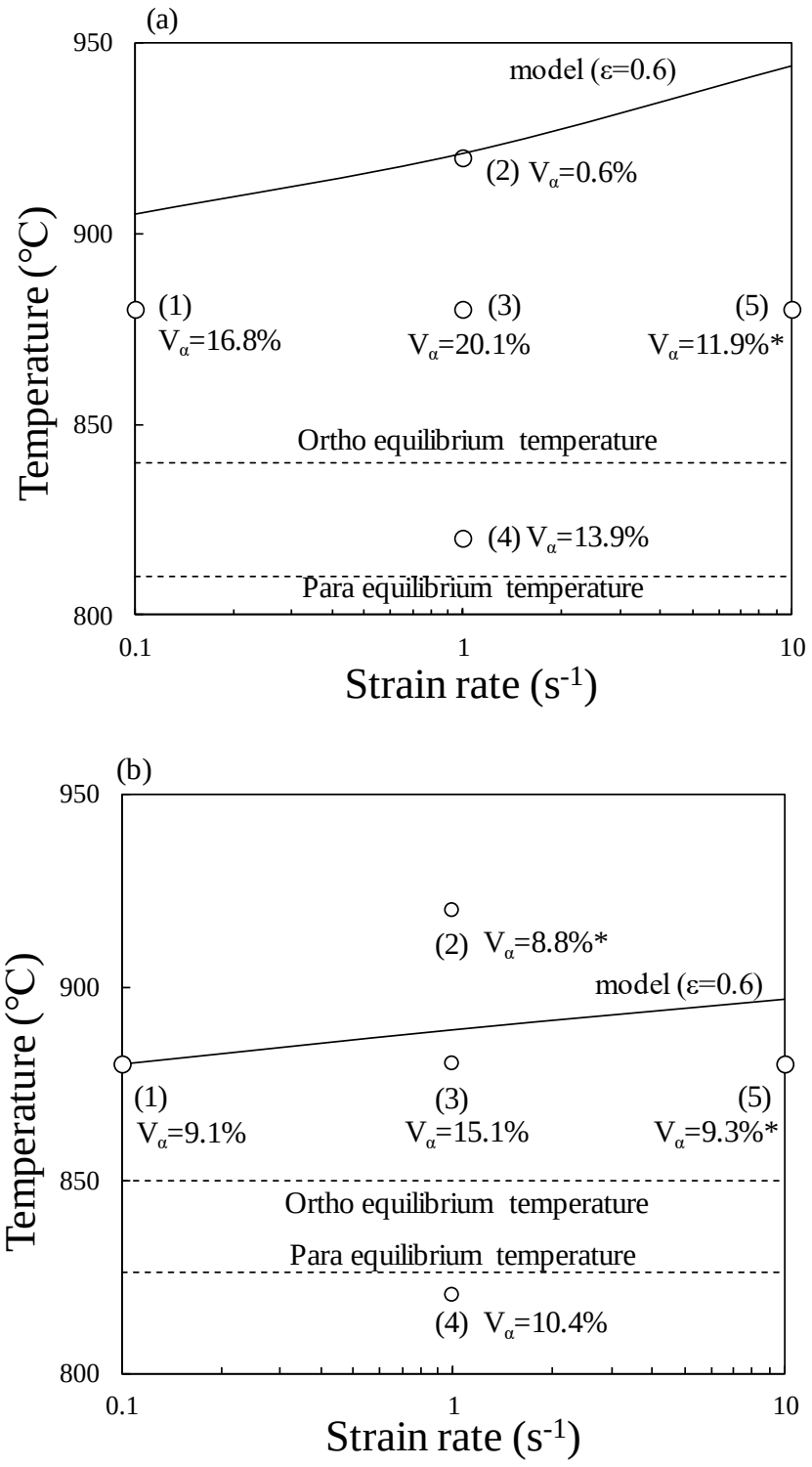

Fig. 6.1 Comparison of model calculation and ferrite fraction of (a)Steel A (Fe–C–Mn–0.9 wt% Si), and (b)Steel B (Fe–C–Mn–0.5 wt% Si). A mark (*) shows unreliable results.

6.3 Mechanism of Widmanstätten ferrite transformation

A possible mechanism wherein the ferrite transforms to a needle shape and initiated at the grain boundaries is illustrated in **Fig. 6.2**. When deformation is applied to austenite grains shear bands can form. Because the strain from the deformation is not uniform, the strain is concentrated in the shear bands which will intersect the grain boundaries. The intersection between the grain boundaries and the shear bands would be one of the most favorable initiation sites for the dynamic ferrite. In addition, since the shear bands are thin in nature, the dynamic ferrite grows as a plate along the shear band and results in the Widmanstätten morphology.

Consequently, when the deformation is applied to the austenite grain, the needle shaped ferrite forms in the grain boundaries.

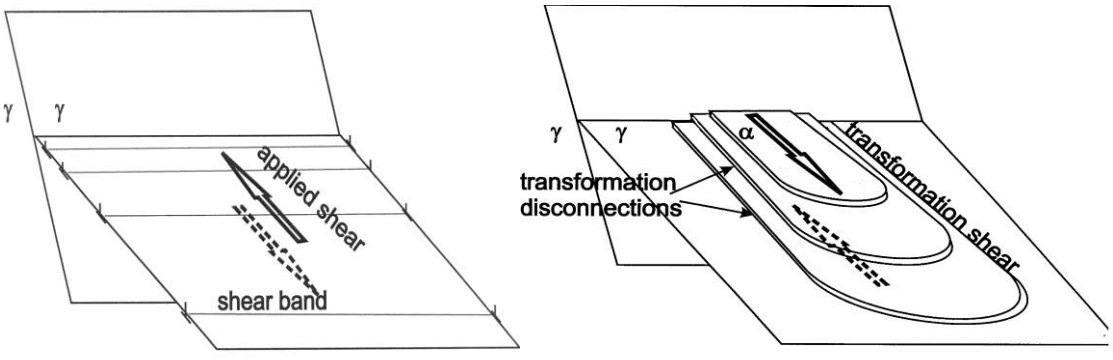

Fig. 6.2 Mechanism of the ferrite formation.

6.4 Effect of the dynamic recrystallization

Some dilatometry results related to the strain rate were not able to be explained in section 6.2. One possible reason for explaining these experimental results is dynamic recrystallization. Static recrystallization takes place when the work hardening structure resulting from deformation is held at high temperature. On the other hand, dynamic recrystallization happens during deformation at high temperature. As shown in **Fig. 6.3**, the stress–strain curves for a material which undergoes dynamic recrystallization generally exhibit a broad peak that is different from the plateau. For a strain of 0.6, it is very likely that significant dynamic recrystallization takes place at higher strain rates, and dynamic recrystallization competes with the softening mechanism of the dynamic transformation. If dynamic recrystallization takes place on the austenite grain boundaries or shear bands, it can eliminate the nucleation sites for the dynamic transformation ferrite. This can affect the volume fraction of ferrite. Nonetheless, what we can get out of this diagram is an indication of whether or not the dynamic ferrite will form. These results seem to be in good agreement with the model. When we fit the stress-strain curve, the effect of the work hardening, dynamic recovery or dynamic recrystallization were not included. Thus the experimental flow stress curve is lower than that predicted by the calculation at higher strain rates, as shown in **Fig. 5.1d**.

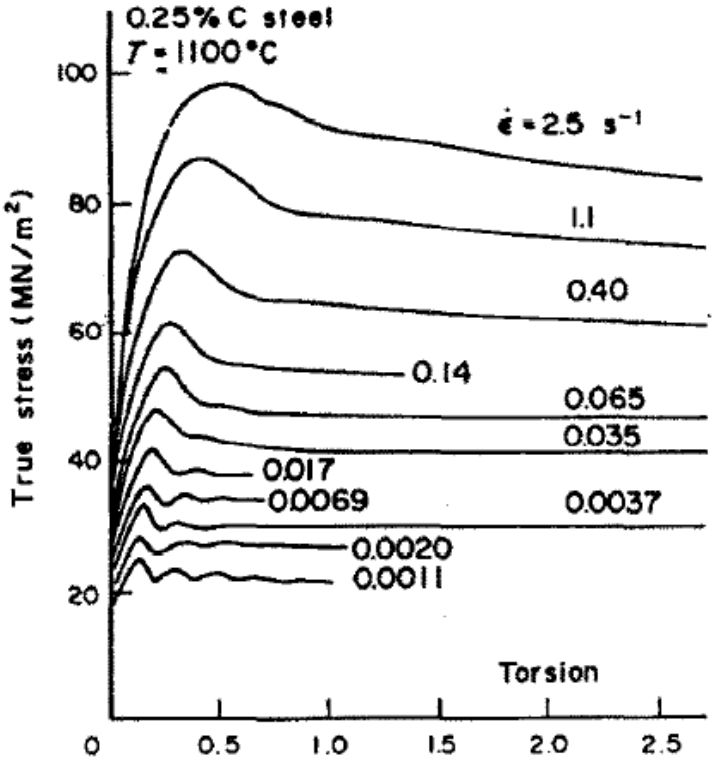

Fig. 6.3 Influence of strain rate on the flow curves at 1100°C for a 0.25 wt%C steel (Rossard & Blain 1959).

6.5 Shortcoming for observing dilatation

As shown in **Fig. 6.1**, based on the model predictions, we expected less dynamic ferrite in Steel B. However, the dilatometer results show that point No.2 has a surprisingly high volume fraction of ferrite. This highlights that there are some shortcomings in using dilatation measurements.

Our method to observe the dynamic transformation relies on the indirect source of the dilatometer, and this leads to two possible uncertainties. First, the length

contraction might progress after 10 seconds holding time. As shown in **Fig. 5.15**, these signals decrease just before 10 seconds. If the holding time was longer, more contraction could be observed. Second, the dilatation signal peaks after the initial second, and thus we thought that the contraction starts beginning at this peak, as shown in **Fig. 5.14**. It is possible that this peak could be generated as a result of a combination of the length contraction from the reverse transformation and an expansion from an unknown effect, as shown in **Fig. 6.4**. The increase of this unknown signal is much faster than length contraction because the reverse transformation from ferrite to austenite is a diffusional transformation. If this unknown signal is much bigger than the contraction, the dilatometer signal could increase gradually, as shown in **Fig. 5.11** for the sample held at 820°C. Hence, it is difficult to accurately estimate the volume fraction of ferrite from length change and to quantify the ferrite fraction because we assume a monotonic decrease when calculating the ferrite volume fraction, but the dilatation data sometimes peaks. Nonetheless, the experiments qualitatively show clear evidence of the dynamic transformation because the contraction is observed.

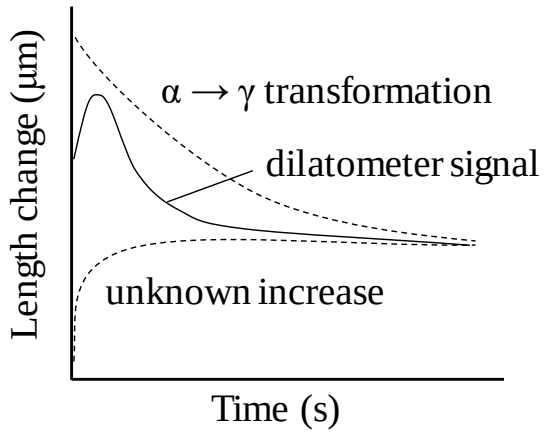

Fig. 6.4 Schematic diagram of the composition of the dilatometry data.

6.6 Dynamic transformation in the industrial processing

Industrial hot strip mill data obtained from US Steel Canada is shown in **Fig. 6.5**. All of this data was measured during roughing and finishing mill processing for the commercial steel with the same composition as Steel A in **Table 4.1**. It can be seen in **Fig. 6.5a** that the temperature drops down periodically by approximately 25 °C. The plate length after going through the roughing mill was approximately 100 m, and the slab length before rolling was about 10 m. Hence, the slab length elongated about ten times. On the other hand, as can be seen in **Fig. 6.5a**, the length between each cooling point is approximately 20 m, which is equivalent to around 2 m in the original slab. This length of 2 m corresponds to the distance of the skid, which is a supporting bar cooled with water in the reheating furnace. The important of this is that this cold spot later became a hot spot as shown in **Fig. 6.5c**. In addition, as shown in **Fig. 6.5b**, the thickness

of the strip decreases as the hot spot. Therefore, the as a result of the skid marks the mill is likely unable to produce uniform steel sheets in terms of the property and the thickness.

The temperature versus strain for each finishing mill is represented in **Fig. 6.6**. Here it can be seen that the strain is greatest towards the beginning of the finishing process with a brief drop in strain at the F2 stand. After increasing for the F3 stand, the strain continuously drops at a steady rate for the subsequent stands. Between F4 and F6 is where the temperature reversal is expected to occur. It is worth nothing that between these stages the applied deformation ranged between 0.25 to 0.4.

A schematic diagram of the temperature reversal mechanism is shown in **Fig. 6.7**. When the steel exits the reheating furnace, the skid marks are approximately 25 °C colder than the surrounding slab. After the F4 stand, the steel continues to have the cold spots that directly correspond to the skid marks from the reheating furnace. After exiting the F5 stand, an exothermic austenite to ferrite reaction occurs in the colder skid regions. This is why after the F5 stand a more uniform temperature reading was observed in the steel. It is assumed that the surrounding slab is fully austenitic at this point with no dynamic transformation ferrite yet. After exiting F6, a temperature reversal occurs where the once cold spots are now higher in temperature. Since the growth of ferrite is

an exothermic process, this will cause the cold spots to increase in temperature. Therefore, it is likely that the dynamic transformation could happen in the industrial processing of steel, and that this phenomenon could be affect the ability of the mill to make uniform products.

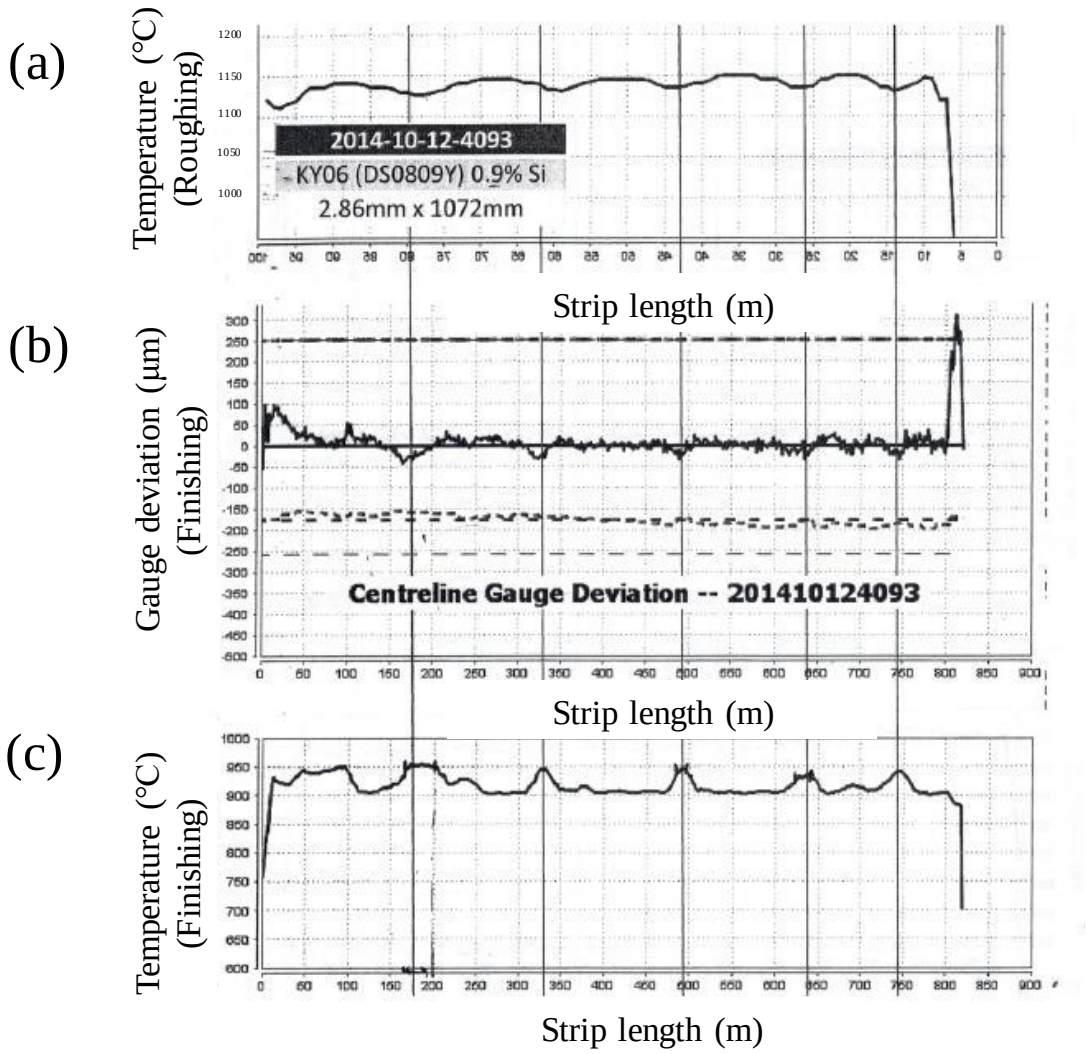

Fig. 6.5 Temperature and gauge length deviations (with respect to thickness) for material exiting the roughing and finishing mills. The material is the same composition as Steel A.

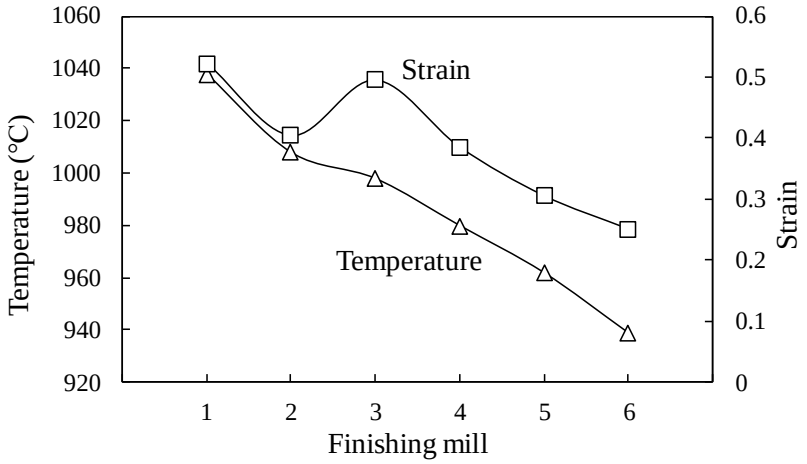

Fig. 6.6 Temperature and strain for finishing mill

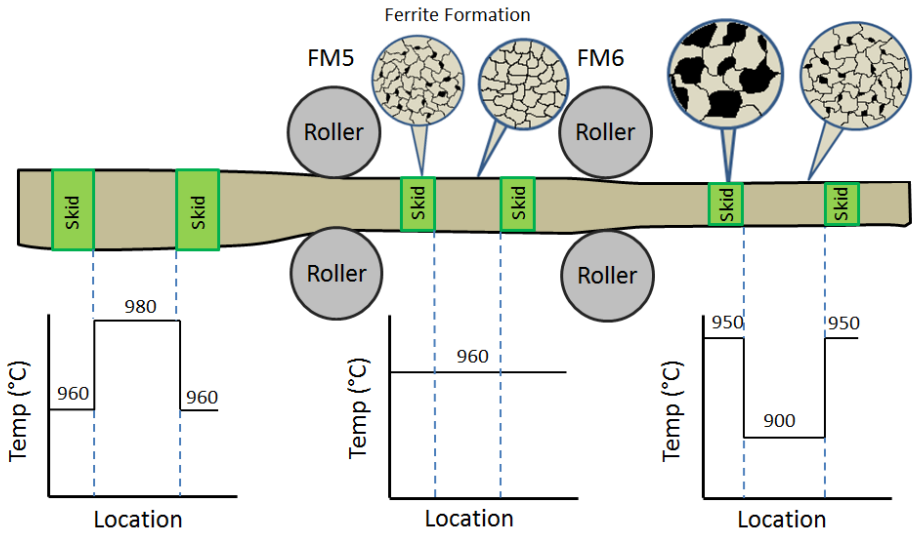

Fig. 6.7 Temperature reversal between finishing mills 4 to 6.

Chapter 7. Conclusions

A dynamic transformation model was established which includes the driving force, which is dependent on the internal back stress, and also includes the opposing force, which considers carbon diffusion.

In this work, to verify the model, hot compression experiments using samples of two different kinds of alloys were carried out. The deformation dilatometer was used in these experiments to measure the length change that resulted from the reverse transformation of the dynamic transformation ferrite to austenite.

The samples belonging to the Fe–Mo–C system were used to compare the volume fraction of ferrite between the dilatometry data and the optical micrographs. The ferrite fraction from the optical metallography was found to be a significantly larger amount of ferrite than the dilatometry results. An EBSD image at lower temperature showed that Widmanstätten ferrite and polygonal ferrite were both observed. This result suggests that, at higher temperatures, polygonal ferrite could be generated during quenching because the dislocations from deformed austenite could be sites for the nucleation of additional ferrite. Therefore, the dilatometry data is believed to be a more reliable measure.

The other samples were from the Fe–C–Mn–Si system, which is a commercial steel. According to the model, at higher strain rates, more dynamic transformation takes place. However, the dilatometer results showed lower ferrite precipitation for conditions using highest strain rate when compared to the results for an intermediate strain rate. It is likely that at the highest strain rate dynamic recrystallization takes place and consequently affects the sample dilatation. In addition, since the method for observing the volume fraction from the dilatation has a few shortcomings, it is difficult to accurately estimate the volume fraction of ferrite from length change and to quantify the ferrite fraction.

According to the manufacturing process data, some hot spots appeared on steel sheets after the finishing mill. The likely mechanism is that cold spots on these slabs called skid marks can transform to ferrite earlier than the surrounding slab during deformation. Because the cold spots are close to the Ae3 temperature, the dynamic transformation can take place. As a result of this dynamic transformation, the exothermic phenomenon of the ferrite growth causes the hot spots on the steel sheets to appear.

Chapter 8. Future Work

In the course of this investigation, several new ideas have emerged for further exploring the formation of dynamic ferrite and gaining a better insight into the mechanism for ferrite formation under an applied load. The first group of proposed experiments will utilize in-situ techniques. In order to achieve direct observation of the formation of dynamic ferrite it would be helpful to perform experiments using a synchrotron beam on compression samples deformed in-situ above the Ae3 temperature. This experiment would also quantification of ferrite volume fraction and the kinetics of ferrite reversion during isothermal holding once the applied stress is removed. If the application is successful, the experiments could be carried out for different alloy compositions in order to assess the effect of the thermodynamic opposing force on the transformation. Other in-situ experiments, that could be carried out, include observing the deformation using a confocal microscope. In this case, Widmanstätten ferrite might be visible due to surface relief. While this method will not provide direct crystallographic evidence for ferrite formation, it could provide information on the locations at which the ferrite plates form and their morphology. Hot-deformation of the samples within an SEM which is equipped with an EBSD detector could be used to provide both crystallographic and morphological

information. The feasibility of this experiment will depend on the configuration of the EBSD detector and whether the area of interest can be scanned rapidly prior to the reversion of ferrite to austenite.

In addition to the above in-situ experiments, there are a number of ex–situ experiments that could be carried out to provide direct observation of the morphology and volume fraction of the ferrite formed by dynamic transformation. In particular, one could exploit the temperature range between the PE (para equilibrium limit) and Ae3 temperature. This temperature range is interesting because isothermal precipitation of ferrite above the PE temperature can only take place under full partitioning condition. Since the partition (diffusion) of substitutional elements is very slow, ferrite formation would not be expected for short heat–treatments. Thus the formation of ferrite under deformation conditions above PE would only be possible as a result of the dynamic transformation mechanism. Interestingly, however, one would not expect all the ferrite formed above the PE limit and below the Ae3 limit to revert to austenite because there is a stable equilibrium fraction of ferrite at this temperature. We observed evidence of this in the dilatometer experiments. In these experiments, the signal from ferrite reversion was smaller when the deformed material was isothermally held at a temperature between the PE and Ae3 temperatures. Thus

deformation in this temperature range might provide opportunities to retain some of the dynamic ferrite on quenching and observe it by optical metallography or EBSD. This might be most effective in alloys with very high hardenability such as Mo containing alloys and medium Mn alloys (e.g. with 6%Mn).

If one is able to reliably retain some of the dynamic ferrite on quenching, several additional studies could be carried out to confirm the mechanism by which the phase transformation takes place. For example, one could carry out EBSD reconstruction of the former austenite grains and check whether the observed Widmanstätten ferrite plates are those expected based on the maximum Schmidt factor argument. This experiment is best applied to a material with very strong texture in order to simplify the analysis.

Other experiments that would be valuable for understanding the mechanism by which dynamic ferrite forms include ones in which the strain-rate is varied in order to better understand the range of conditions under which the transformation is controlled by carbon diffusion. If carbon diffusion is very fast, then the transformation is limited by the mobility of the disconnections and one would expect that the transformation will be accelerated with increasing deformation rate (larger driving force). If carbon

diffusion is the rate limiting step, then it is possible to have situations in which increasing the deformation rate does not accelerate the transformation.

It is also worth carrying experiments on materials with low stacking fault energy (e.g. high Mn steels) in order to reduce recovery and promote planar slip. This would strongly favor the formation of Widmanstätten ferrite along deformation bands as suggested in this work. The use of high Mn steel might also be interesting because of the possibility of retaining the austenite after cooling to room temperature.

Bibliography

Aranas, Jr, C. et al., 2015. Flow Softening-based Formation of Widmanstätten Ferrite in a 0 . 06 % C Steel Deformed Above the Ae 3. , 55(1), pp.300–307.

Aranas, Jr, C. & Jonas, J.J., 2015. Effect of Mn and Si on the dynamic transformation of austenite above the Ae3 temperature. *Acta Materialia*, 82, pp.1–10.

Basabe, V. V, Jonas, Ã.J.J. & Ghosh, C., 2014. Formation of Widmansta ¨ tten Ferrite in a 0 . 036 % Nb Low Carbon Steel at Temperatures Above the Ae 3. , 85(1), pp.8–15.

Beladi, H., Kelly, G.L. & Hodgson, P.D., 2004. Formation of Ultrafine Grained Structure in Plain Carbon Steels Through Thermomechanical Processing. , 45(7), pp.2214–2218.

Bhadeshia, H.K.D.H., 2001. *Bainite in steels* 2nd ed., University of Cambridge, Institute of Materials.

Chen, Y. & Chen, Q., 2003. Dilatometric investigtion on isothermal transformation after hot deformation. *Journal of Iron and Steel Research*, 4, pp.46–48.

Dong, H. & Sun, X., 2005. Deformation induced ferrite transformation in low carbon steels. , 9, pp.269–276.

Estrin, Y., 1996. Dislocation-density-related constitutive modeling. In *Unified constitutive laws of plastic deformation*. pp. 69–106.

Frost, H.J. & Ashby, M.F., 1982. *Deformation-Mechanism Maps, The Plasticity and Creep of Metals and Ceramics*,

Garafalo, F., 1963. An empirical relation defining the stress dependence of minimum creep rate in metals. *Trans AIME*, pp.351–355.

Ghosh, C., Basabe, V. V, Jonas, J.J., Yue, S., et al., 2013. Dynamic Transformation

Behavior of a Deformed High Carbon Steel at Temperatures Above the Ae 3. , 53(5), pp.900–908.

Ghosh, C., Basabe, V. V, Jonas, J.J., Kim, Y., et al., 2013. The dynamic transformation of deformed austenite at temperatures above the Ae 3. *Acta Materialia*, 61(7), pp.2348–2362.

Ghosh, C., Basabe, V. V & Jonas, J.J., 2014. Thermodynamics of dynamic transformation of hot deformed austenite in four steels of increasing carbon contents. *Materials Science & Engineering A*, 591, pp.173–182.

Hanlon, D.N., Sietsma, J. & Zwaag, S. Van Der, 2001. The Effect of Plastic Deformation of Austenite on the Kinetics of Subsequent Ferrite Formation. , 41(9), pp.1028–1036.

Hernandez, C.A., Medina, S.F. & Ruiz, J., 1996. Modelling austenite flow curves in low alloy and microalloyed steels. *Acta Materialia*, 44(1), pp.155–163.

Hickson, M.R., 1999. The effect of chemistry on the formation of ultrafine ferrite in steel. *ISIJ International*, 39(1 999), pp.76–80.

Howe, J.M., Pond, R.C. & Hirth, J.P., 2009. Progress in Materials Science The role of disconnections in phase transformations. , 54, pp.792–838.

Jiao, H. et al., 2003. Precipitate orientation relationships and interfacial structures in duplex stainless steel Zeron-100. *Philosophical Magazine*, 83, pp.1867–1887.

Jonas, J.J. & Ghosh, C., 2013. Role of mechanical activation in the dynamic transformation of austenite. *Acta Materialia*, 61(16), pp.6125–6131.

Kocks, U.F., 1976. Laws for Work-Hardening and Low-Temperature Creep. *Journal of Engineering Materials and Technology*.

Kocks, U.F. & Mecking, H., 2003. Physics and phenomenology of strain hardening :

the FCC case. *Progress in Materials Science*, 48, pp.171–273.

Liu, Z. et al., 2007. Thermal Stability of High Temperature Deformation Induced Ferrite in a Low Carbon Steel. *ISIJ International*, 47(2), pp.289–293.

Medina, S.F. & Hernandez, C.A., 1996. General expression of the Zener-Hollomon parameter as a function of the chemical composition of low alloy and microalloyed steels. *Acta Materialia*, 44(1), pp.137–148.

Medina, S.F. & Hernandez, C.A., 1992. Stress-strain curve mathematical modelling of steel. Application to estimate the hot rolling force. *Memoires et etudes scientifiques de la Revue de metallurgie*, 89(4), pp.217–223.

Portet, D., 2009. *Phase transformations in metals and alloys*, Taylor Francis Group.

Priestner, R., 1981. Processing of an International Conference on the Thermomechanical Processing of Microalloyed Austenite. In Metallurgical Society of AIME, p. 455.

Rodrigues, S.F., Jr, C.A. & Jonas, J.J., 2017. Dynamic Transformation during the Simulated Plate Rolling of a 0.09% Nb Steel. *ISIJ International*.

Rossard, C. & Blain, P., 1959. No Title. *Mém. Scient. Rev. Métall.*, p.285.

Senuma, T., 1988. A New Thermomechanical Heat Treatment for Grain Refining in Low Carbon Steels. *Proc. Int. Conf. on Phys. Metallurgy of Thermomechanical Processing of Steels and Other Metals*, pp.200–207.

Sun, X. et al., 2008. Microstructural Evolution and Kinetics for Post-dynamic Transformation in a Plain Low Carbon Steel. , 48(7), pp.994–1000.

Voce, E., 1948. The relationship between stress and strain for homogeneous deformations. *J Inst Metals*, pp.537–562.

Watson, J., 1973. The crystallography of Widmanstatten. *Acta Metall*, 21, pp.961–

973.

Yada, H., Li, C. & Yamagata, H., 2000. Dynamic γ → α Transformation during Hot Deformation in Iron – Nickel – Carbon Alloys. , 40(2), pp.200–206.

Yada, H., Matsumura, Y. & Senuma, T., 1986. Massive type transformation indeced by hot deformation in low carbon steels. *Proceedings of the international conference on martensitic transformation*, pp.515–520.

Zener, C. & Hollomon, J.H., 1944. Effect of Strain Rate Upon Plastic Flow of Steel Contributed Original Research. , 22(1944).